Chapter 2
Seismic Response of Rail-Counterweight System

This chapter focuses on the analytical study of a rail-counterweight system exposed to seismic motions. Previous analytical and experimental studies done on this system are reviewed. The deficiencies in the models used in these studies are noted. The rest of the chapter is then devoted to describe the development of the analytical model used in this study including the effect of system nonlinearities, and then evaluate the seismic performance of the system under several recorded and synthetically generated accelerograms. The performance of the system is evaluated in terms of overstressing of the rails and bracket supports, and also in terms of the system fragility for an ensemble of seismic motions.

2.1 Previous Studies on Rail-Counterweight in Elevators

The observed seismic damages on elevators, especially the rail-counterweight system, have been followed by a continued research interest on the seismic response characteristics and performance of elevators in buildings. As most of the damage happened to the rail-

counterweight systems, most of the studies were focused on the dynamic behavior of the rail-counterweight system.

Yang et al. (1983) studied the nonlinear response of physical model of counterweight subjected to harmonic excitation in the in-plane direction and compared the results with those of finite element method. The counterweight model consisted of two end plates connected by a central member and two flexible members representing the frame, and five small shafts attached perpendicular to the central member representing the weights. The weights were free to slide within the counterweight frame. The counterweight was supported by a leaf spring at each of its corner, simulating the roller guide assemblies. The rails were represented by two steel bars with rectangular cross sections. In the finite element model, the rails were modeled as simply supported beams and the counterweight frame was modeled as beam on elastic supports. The springs that connected the counterweight and the rail were assumed to behave as bilinear springs, which had zero values when there was no contact and very large value when they were in contact. Because of difference in the physical characteristics between the two methods, only the general forms of the responses were compared.

Tzou and Schiff (1984, 1989) used similar model to evaluate the dynamic loading due to contact between the weights and the frame. The rail and the counterweight frame were modeled as a single combined beam. The counterweight was assumed to be located in the middle of the rail span. A large separation was provided between the weight and the frame. It was found that the seismic response of the counterweight can be improved by providing a large separation so that contact was avoided. However, when contact did happen, the response was worse than that of the regular small gap. One modification that was suggested if contact occurred was installation of rubber damper between the frame and the weights. It was

concluded that the rubber dampers could decrease the rail load provided that proper values of coefficients were selected.

Segal et al. (Segal et al. 1994, 1995, 1996; Rutenberg et al. 1996; Levy et al. 1996) studied the seismic response of counterweight modeled as two independent mass located at the upper and lower guiding members. The counterweight was guided along the rail by sliding shoes. Therefore, it hanged freely before contact happened. Contact elements were used to represent rail-brackets system, using parallel combination of spring, dashpot, and Coulomb friction element. The vertical velocity of the counterweight was included in the analysis. Because of the Coulomb friction element, which would come into the equations when contact occurred, different vertical velocity would result in different equivalent stiffness of the rail. An ensemble of recorded earthquake ground motion normalized to 0.4 m/s and 0.3 m/s peak ground velocities were used an input motion to the building. All bracket supports were assumed to be subjected to the same acceleration equal to that at the top of the building.

In all these previous studies, not much attention was given to the proper modeling of the rail-counterweight systems, especially of their roller guide assemblies. In some respect their models were different from each other. Suarez and Singh (1996, 1998) were perhaps the first one to include the details of the roller guide assembly in the preparation of their analytical model. To study the out-of-plane motion of the counterweight, they used three-degrees-of-freedom model which included equivalent springs representing the roller guide assemblies, rails, and bracket supports. The continuous beam effect of the rail was also included. In the first study, the model was reduced to a single degree-of-freedom system by relating the frequencies of the rotation modes to the translation mode, and response spectrum approach was used to calculate the response. In the second paper, the effect of saturation of the roller

guide was included. This model also ignored several important features of the counterweight systems used in elevators, for example, the code limits on the clearances between the restraining plates at the roller guide assemblies and clearance between the counterweight frame and the rail.

2.2 Analytical Model for Rail-Counterweight System

In this study, the counterweight frame is modeled as a rigid block of height l_c, width d, and depth e. The weights fill the bottom two-third of the frame and the center of mass of the counterweight is located at a distance l_m from the bottom of the frame, as shown in figure 2.1. The flexibility of the system is provided by the combination of brackets, guide rails, and roller guide assemblies, represented by an equivalent spring at each of the four corners of the counterweight frame. The stiffness of the supporting system of the counterweight is obtained by taking into account the continuous rails on bracket supports and the stiffness of the roller guide assembly. The values of the combined stiffness could be different for the upper and lower roller guides depending upon their locations on the guide rails.

The dynamic motions of the counterweight under seismic load can be described in five degrees of freedom, two translations u and v, and three rotations ψ, θ, and ϕ, as also shown in figure 2.1. The degrees of freedom u and ψ are associated with in the in-plane motion of the counterweight while others are associated with the out-of-plane motion. The equations of motion for these two directions are developed separately in the following sections.

2.2.1 Sources of Nonlinearities

There are several sources that can introduce nonlinearity to the rail-counterweight system during its vibrations. The first source is the force-deformation characteristics of the tires of the roller guide. The nonlinear behavior of the tires can be established in a reliable manner only

through experiments. However, as shown by Diaz (1999), within the range of deformation during earthquake-induced vibration the force-deformation relationship can be assumed to be linear.

Yielding of the rails or brackets due to excessive stress can also cause nonlinearity in the system. However, the post-yielding behavior of the rail-counterweight system is not much of practical interest since the damage would have been permanent. In fact, the main objective of the study is to avoid this failure.

Saturation of the helical spring in the roller guide assembly when the deformation close the gaps between helical wire loops can also introduce nonlinearity to the system. This can be avoided by proper design of the spring. Moreover, if this saturation occurs before the contact between restraining plate and the rail it can be included in the analysis by modifying the force-deformation characteristics associated with the contact.

The sources of nonlinearity that are included in this analysis are associated with closing of the gap between the restraining plated and the rails at any of the four roller guide assemblies and between the counterweight frame and the rail at the bracket support. As mentioned earlier in Chapter 1, a restraining plate is provided at each roller guide assembly to avoid roller guide coming off the guide rails during earthquake. The code requires a maximum clearance of 3/16 inches between the restraining plate and the rail in both in-plane and out-of-plane directions. This gap is shown in Figure 1.4 in Chapter 1. During the earthquake-induced vibration, this gap could possibly be closed especially under medium or strong ground motion. When contact between one of the restraining plates and the rail happens, the flexibility will be provided only by the guide rail and the supporting bracket. Because the springs representing the roller guide assemblies and rail-brackets are in series

with each other, and the guide rails and brackets are much more rigid than the helical springs and rubber tires, the stiffness of the system will increase significantly after the contact. Therefore, the force-deformation relationship of the equivalent spring at each corner can be represented by bilinear diagram as shown in Figure 2.2.

The middle, almost flat, part of the diagram represents the equivalent spring before contact happens when the tangent stiffness k_t is governed by the roller guide assembly. On the steep portion of the diagram, the tangent stiffness k_t' is governed by that of the guide rail and bracket. The relationship between the force f and deformation δ can then be written as

$$f = k\delta - \delta_m \Delta k \operatorname{sgn}(\delta) \tag{2.1}$$

where

$$k = \begin{cases} k_t & \text{if } |\delta| \le \delta_m \\ k_t' & \text{if } |\delta| > \delta_{\mathrm{m}} \end{cases} \tag{2.2}$$

$$\Delta k = k_t' - k_t \tag{2.3}$$

δ_m is the maximum deformation before contact happens, and sgn is the sign function that returns the value of –1 if $\delta < 0$, 0 if $\delta = 0$, or 1 if $\delta > 0$.

During the in-plane motion of the rail-counterweight system, one of each pair of rollers at the upper and lower roller guide assemblies will always be in contact with the rail, providing the restoring forces f_u and f_l. Using (2.1), these forces can be written as

$$\begin{Bmatrix} f_u \\ f_l \end{Bmatrix} = \begin{bmatrix} k_{iu} & 0 \\ 0 & k_{il} \end{bmatrix} \begin{Bmatrix} u_u \\ u_l \end{Bmatrix} - u_m \begin{Bmatrix} \Delta k_{iu} \operatorname{sgn}(u_u) \\ \Delta k_{il} \operatorname{sgn}(u_l) \end{Bmatrix} \tag{2.4}$$

where u_u and u_l is the in-plane displacement of the equivalent spring at the upper and lower supports of the frame, respectively, and u_m is the maximum displacement before contact happens. Unless otherwise noted, subscripts u and l will be used throughout this thesis to

respectively denote the upper and lower part of the counterweight frame. Similarly, subscripts *i* and *o* will denote the values in the in-plane and out-of-plane directions, respectively.

For the out-of-plane direction, all equivalent spring at the four corners of the frame contribute in providing the elastic force as follows

$$\begin{Bmatrix} f_{u1} \\ f_{u2} \\ f_{l1} \\ f_{l2} \end{Bmatrix} = \begin{bmatrix} k_{ou1} & 0 & 0 & 0 \\ 0 & k_{ou2} & 0 & 0 \\ 0 & 0 & k_{ol1} & 0 \\ 0 & 0 & 0 & k_{ol2} \end{bmatrix} \begin{Bmatrix} v_{u1} \\ v_{u2} \\ v_{l1} \\ v_{l2} \end{Bmatrix} - v_m \begin{Bmatrix} \Delta k_{ou1} \operatorname{sgn}(v_{u1}) \\ \Delta k_{ou2} \operatorname{sgn}(v_{u2}) \\ \Delta k_{ol1} \operatorname{sgn}(v_{l1}) \\ \Delta k_{ol1} \operatorname{sgn}(v_{l2}) \end{Bmatrix} \tag{2.5}$$

The code also limits the gap between the counterweight and the frame to be not more than half of an inch. If the combined deformations of the guide rail and the roller guides at the two ends are large enough to overcome this gap, the bracket support will provide another resisting force for the in-plane motion of the rail-counterweight system. The force-deformation diagram for this case is shown in figure 2.3.

This can happen only when the upper and lower roller guides are located on the upper and lower sides of a bracket support, respectively. In other words, the position of the counterweight is such that

$$a_u > L - l_c \tag{2.6}$$

where a_u is the distance from the upper roller guide to the next bracket support above it, L is the story height (or distance between two consecutive bracket supports), and l_c is the height of the counterweight.

The force f_s can be calculated from

$$f_s = k_{br}\left(u_s - u_{sm} \operatorname{sgn}(u_s)\right) \tag{2.7}$$

where u_s is the in-plane displacement of the counterweight at the bracket support level, u_{sm} is the maximum displacement before contact happens, and

$$k_{br} = \begin{cases} k_{br-inplane} & \text{if } a_u > L - l_c \text{ and } |u_s| > u_{sm} \\ 0 & \text{otherwise} \end{cases} \tag{2.8}$$

represents the tangent stiffness of the force-deformation diagram that is provided by the bracket.

Combining (2.4) and (2.7), the restoring force vector in the in-plane direction becomes

$$\begin{Bmatrix} f_u \\ f_l \\ f_s \end{Bmatrix} = \begin{bmatrix} k_{iu} & 0 & 0 \\ 0 & k_{il} & 0 \\ 0 & 0 & k_{br} \end{bmatrix} \begin{Bmatrix} u_u \\ u_l \\ u_s \end{Bmatrix} - \begin{Bmatrix} u_m \Delta k_{iu} \operatorname{sgn}(u_u) \\ u_m \Delta k_{il} \operatorname{sgn}(u_l) \\ u_{sm} k_{br} \operatorname{sgn}(u_s) \end{Bmatrix} \tag{2.9}$$

2.2.2 In-Plane Motion

Figure 2.4 shows the three forces and the inertial forces acting in the in-plane direction. Using the balance of force along the x-axis and moment about the y-axis, we obtain

$$-(f_u + f_l + f_s) = m_c (\ddot{u}_c + \ddot{x}_c) \tag{2.10}$$

$$-f_u (l_c - l_m) - f_s (l_c - l_m - l_s) + f_l \, l_m = J_\psi (\ddot{\psi} + \ddot{\delta}) \tag{2.11}$$

where l_s is the distance between the upper roller guide to the contact location at the bracket support level

$$l_s = L - a_u \tag{2.12}$$

and

$$J_\psi = \frac{m_c l_m^2}{3} \left(1 + \frac{d^2}{4 l_m^2} \right) \tag{2.13}$$

Introducing new variables

$$u_e = l_m \psi \tag{2.14}$$

$$\ddot{x}_e = l_m \ddot{\delta} = \frac{l_m}{l_c}\left(\ddot{x}_u - \ddot{x}_l\right) \tag{2.15}$$

equations (2.10) and (2.11) can be written in matrix form

$$\boldsymbol{M_i}\ddot{\boldsymbol{q}}_{\boldsymbol{i}} + \boldsymbol{F_i} = -\boldsymbol{M_i}\ddot{\boldsymbol{x}} \tag{2.16}$$

where

$$\boldsymbol{M_i} = m_c \begin{bmatrix} 1 & 0 \\ 0 & \gamma_1 \end{bmatrix} ; \quad \boldsymbol{q_i} = \begin{Bmatrix} u \\ u_e \end{Bmatrix} ; \quad \ddot{\boldsymbol{x}} = \begin{Bmatrix} \ddot{x}_c \\ \ddot{x}_e \end{Bmatrix} \tag{2.17}$$

$$\boldsymbol{F_i} = \begin{bmatrix} 1 & 1 & 1 \\ \frac{l_c}{l_m} - 1 & -1 & \frac{l_c}{l_m} - 1 - \frac{l_s}{l_m} \end{bmatrix} \begin{Bmatrix} f_u \\ f_l \\ f_s \end{Bmatrix} = \boldsymbol{T_i^T} \begin{Bmatrix} f_u \\ f_l \\ f_s \end{Bmatrix} \tag{2.18}$$

$$\gamma_1 = \frac{1}{3}\left(1 + \frac{d^2}{4l_m^2}\right) \tag{2.19}$$

The displacement vector in (2.9), which contains the displacement at the upper and lower roller guide as well as at the possible contact location between the frame and the rail, can be related to the degrees of freedom of the system $\boldsymbol{q_i}$ with transformation matrix $\boldsymbol{T_i}$ as follows

$$\begin{Bmatrix} u_u \\ u_l \\ u_s \end{Bmatrix} = \begin{bmatrix} 1 & \frac{l_c}{l_m} - 1 \\ 1 & -1 \\ 1 & \frac{l_c}{l_m} - 1 - \frac{l_s}{l_m} \end{bmatrix} \begin{Bmatrix} u_c \\ u_e \end{Bmatrix} = \boldsymbol{T_i}\boldsymbol{q_i} \tag{2.20}$$

Substituting equations (2.20) and (2.9) into (2.18), the elastic force can be expressed in terms of the tangent stiffness matrix and the nonlinear force component

$$\boldsymbol{F_i} = \boldsymbol{K_{it}}\boldsymbol{q_i} - \boldsymbol{f_i} \tag{2.21}$$

where

$$\boldsymbol{K}_{it} = \boldsymbol{T}_i^T \begin{bmatrix} k_{iu} & 0 & 0 \\ 0 & k_{il} & 0 \\ 0 & 0 & k_{br} \end{bmatrix} \boldsymbol{T}_i \tag{2.22}$$

$$\boldsymbol{f}_i = \boldsymbol{T}_i^T \begin{Bmatrix} u_m \Delta k_{iu} \operatorname{sgn}(u_u) \\ u_m \Delta k_{il} \operatorname{sgn}(u_l) \\ u_{sm} k_{br} \operatorname{sgn}(u_s) \end{Bmatrix} \tag{2.23}$$

The equations of motion (2.16) can now be written as

$$\boldsymbol{M}_i \ddot{\boldsymbol{q}}_i + \boldsymbol{K}_{it} \boldsymbol{q}_i = -\boldsymbol{M}_i \ddot{\boldsymbol{x}} + \boldsymbol{f}_i \tag{2.24}$$

2.2.3 Out-of-plane Motion

The free-body diagram for the out-of-plane motion of the counterweight is shown in figure 2.5. As mentioned earlier, there are four resisting forces at each corner of the frame. The three equations of motion are obtained by summing up forces in the y-direction perpendicular to the plane of the counterweight, and by balancing the moments about the z- and x-axes

$$f_{u1} + f_{u2} + f_{l1} + f_{l2} = -m_c \left(\ddot{v}_c + \ddot{y}_c \right) \tag{2.25}$$

$$-\left[-\left(f_{u1} + f_{u2} \right)\left(l_c - l_m \right) + \left(f_{l1} + f_{l2} \right) l_m \right] = J_\theta \left(\ddot{\theta} + \ddot{\beta} \right) \tag{2.26}$$

$$-\left(f_{u1} - f_{u2} + f_{l1} - f_{l2} \right) \frac{d}{2} = J_\phi \left(\ddot{\phi} + \ddot{\alpha} \right) \tag{2.27}$$

where

$$J_\theta = \frac{m_c d^2}{12} \left(1 + \frac{e^2}{d^2} \right) \tag{2.28}$$

$$J_\phi = \frac{m_c l_m^2}{3} \left(1 + \frac{e^2}{4 l_m^2} \right) \tag{2.29}$$

Following similar procedure as the in-plane motion analysis, we introduce the following response variables

$$v_e = l_m\theta \;\; ; \;\; \ddot{y}_e = l_m\ddot{\beta} \tag{2.30}$$

$$v_e^{'} = \frac{d}{2}\theta \;\; ; \;\; \ddot{y}_e^{'} = \frac{d}{2}\ddot{\alpha} \tag{2.31}$$

and write the equations of motion in matrix form

$$\boldsymbol{M_o}\ddot{\boldsymbol{q}}_{\boldsymbol{o}} + \boldsymbol{F_o} = -\boldsymbol{M_o}\ddot{\boldsymbol{y}} \tag{2.32}$$

where

$$\boldsymbol{M_o} = m_c\begin{bmatrix} 1 & 0 & 0 \\ 0 & \gamma_2 & 0 \\ 0 & 0 & \gamma_3 \end{bmatrix} \;; \quad \boldsymbol{q_o} = \begin{Bmatrix} v_c \\ v_e \\ v_e^{'} \end{Bmatrix} \;; \quad \ddot{\boldsymbol{y}} = \begin{Bmatrix} \ddot{y}_c \\ \ddot{y}_e \\ \ddot{y}_e^{'} \end{Bmatrix} \tag{2.33}$$

$$\boldsymbol{F_o} = \begin{bmatrix} 1 & 1 & 1 & 1 \\ 1-\dfrac{l_c}{l_m} & 1-\dfrac{l_c}{l_m} & 1 & 1 \\ 1 & -1 & 1 & -1 \end{bmatrix}\begin{Bmatrix} f_{u1} \\ f_{u2} \\ f_{l1} \\ f_{l2} \end{Bmatrix} = \boldsymbol{T_o^T}\begin{Bmatrix} f_{u1} \\ f_{u2} \\ f_{l1} \\ f_{l2} \end{Bmatrix} \tag{2.34}$$

$$\gamma_2 = \frac{1}{3}\left(1+\frac{e^2}{4l_m^2}\right) \tag{2.35}$$

$$\gamma_3 = \frac{1}{3}\left(1+\frac{e^2}{d_m^2}\right) \tag{2.36}$$

The displacements of the four equivalent springs can also be related to the displacement vector $\boldsymbol{q_o}$ using transformation matrix $\boldsymbol{T_o}$

$$\begin{Bmatrix} v_{u1} \\ v_{u2} \\ v_{l1} \\ v_{l2} \end{Bmatrix} = \boldsymbol{T_o}\boldsymbol{q_o} \tag{2.37}$$

Combining (2.34), (2.5), and (2.37), the vector force $\boldsymbol{F_o}$ can then be written in terms of tangent stiffness matrix $\boldsymbol{K_{ot}}$

$$\boldsymbol{F_o} = \boldsymbol{K_{ot}}\boldsymbol{q_o} - \boldsymbol{f_o} \tag{2.38}$$

where

$$\boldsymbol{K_{ot}} = \boldsymbol{T_o^T}\begin{bmatrix} k_{ou1} & 0 & 0 & 0 \\ 0 & k_{ou2} & 0 & 0 \\ 0 & 0 & k_{ol1} & 0 \\ 0 & 0 & 0 & k_{ol2} \end{bmatrix}\boldsymbol{T_o} \tag{2.39}$$

$$\boldsymbol{f_o} = v_m \boldsymbol{T_o^T}\begin{Bmatrix} \Delta k_{ou1}\,\mathrm{sgn}(v_{u1}) \\ \Delta k_{ou2}\,\mathrm{sgn}(v_{u2}) \\ \Delta k_{ol1}\,\mathrm{sgn}(v_{l1}) \\ \Delta k_{ol2}\,\mathrm{sgn}(v_{l2}) \end{Bmatrix} \tag{2.40}$$

Using (2.38), the equations of motion can then be written as

$$\boldsymbol{M_o}\ddot{\boldsymbol{q}}_{\boldsymbol{o}} + \boldsymbol{K_{ot}}\boldsymbol{q_o} = -\boldsymbol{M_o}\ddot{\boldsymbol{y}} + \boldsymbol{f_o} \tag{2.41}$$

In the numerical integration, the equations of motion for the in-plane motion and for out-of-plane motion are combined into

$$\boldsymbol{M}\ddot{\boldsymbol{q}} + \boldsymbol{K_t}\boldsymbol{q} = -\boldsymbol{M}\ddot{\boldsymbol{Y}} + \boldsymbol{f} \tag{2.42}$$

where

$$\boldsymbol{M} = \begin{bmatrix} \boldsymbol{M_i} & \boldsymbol{0} \\ \boldsymbol{0} & \boldsymbol{M_o} \end{bmatrix};\quad \boldsymbol{K_t} = \begin{bmatrix} \boldsymbol{K_{it}} & \boldsymbol{0} \\ \boldsymbol{0} & \boldsymbol{K_{ot}} \end{bmatrix} \tag{2.43}$$

$$\boldsymbol{q} = \begin{Bmatrix} \boldsymbol{q_i} \\ \boldsymbol{q_o} \end{Bmatrix} \tag{2.44}$$

$$\ddot{\boldsymbol{Y}} = \begin{Bmatrix} \ddot{\boldsymbol{x}} \\ \ddot{\boldsymbol{y}} \end{Bmatrix} \tag{2.45}$$

2.2.4 Damping Mechanism

The equations of motion in the previous sections were derived without any damping mechanism in the system. In this study, a viscous damping matrix is added to incorporate some inevitable energy dissipation in the system. The damping matrix is defined in terms of constant modal damping ratio as

$$\boldsymbol{C} = 2\zeta \boldsymbol{M}\boldsymbol{\Phi}\boldsymbol{\omega}_j\boldsymbol{\Phi}^T\boldsymbol{M} \tag{2.46}$$

where ζ is the modal damping ratio, $\boldsymbol{\Phi}$ is the matrix of eigenvectors, and $\boldsymbol{\omega}_j$ is the diagonal matrix of the system frequencies. The final form of the equations of motion with the damping matrix included becomes

$$\boldsymbol{M}\ddot{\boldsymbol{q}} + \boldsymbol{C}\dot{\boldsymbol{q}} + \boldsymbol{K}_t\boldsymbol{q} = -\boldsymbol{M}\ddot{\boldsymbol{Y}} + \boldsymbol{f} \tag{2.47}$$

2.2.5 Input Motion

The acceleration inputs in the equations of motion come from the ground acceleration that is filtered by the building structure. Therefore, the input acceleration vector $\ddot{\boldsymbol{Y}}$ can be expressed in terms of the absolute accelerations of the building floors. For a torsional building, each floor has three components of accelerations: translation in two perpendicular directions $\ddot{U}_n$ and $\ddot{V}_n$, and rotation $\ddot{\Theta}_n$. When the upper roller guides are located between the *n*-th and (*n*-1)-th floors, the accelerations at the roller guides position can be obtained from linear interpolation of accelerations of both floors

$$\ddot{x}_u(t) = \left(1 - \frac{a_u}{L}\right)\left(\ddot{U}_n - y_1\ddot{\Theta}_n\right) + \frac{a_u}{L}\left(\ddot{U}_{n-1} - y_1\ddot{\Theta}_{n-1}\right) \tag{2.48}$$

$$\ddot{y}_{u1}(t) = \left(1 - \frac{a_u}{L}\right)\left(\ddot{V}_n + x_1\ddot{\Theta}_n\right) + \frac{a_u}{L}\left(\ddot{V}_{n-1} + x_1\ddot{\Theta}_{n-1}\right) \tag{2.49}$$

$$\ddot{y}_{u2}(t)=\left(1-\frac{a_u}{L}\right)\left(\ddot{V}_n+x_2\ddot{\Theta}_n\right)+\frac{a_u}{L}\left(\ddot{V}_{n-1}+x_2\ddot{\Theta}_{n-1}\right) \tag{2.50}$$

where x_1, x_2, and y_1 are the distances from the center of mass of the floor to the guide rails as shown in figure 2.6.

The lower roller guides can be located on the same span of rail or on the next span below. When the counterweight is located within a single span of the rail, the accelerations at the lower roller guides are calculated from

$$\ddot{x}_l(t)=\left(1-\frac{a_l}{L}\right)\left(\ddot{U}_n-y_1\ddot{\Theta}_n\right)+\frac{a_l}{L}\left(\ddot{U}_{n-1}-y_1\ddot{\Theta}_{n-1}\right) \tag{2.51}$$

$$\ddot{y}_{l1}(t)=\left(1-\frac{a_l}{L}\right)\left(\ddot{V}_n+x_1\ddot{\Theta}_n\right)+\frac{a_l}{L}\left(\ddot{V}_{n-1}+x_1\ddot{\Theta}_{n-1}\right) \tag{2.52}$$

$$\ddot{y}_{l2}(t)=\left(1-\frac{a_l}{L}\right)\left(\ddot{V}_n+x_2\ddot{\Theta}_n\right)+\frac{a_l}{L}\left(\ddot{V}_{n-1}+x_2\ddot{\Theta}_{n-1}\right) \tag{2.53}$$

If the counterweight is located on two consecutive spans, the lower roller guides will be between the (n-1)-th and (n-2)-th floors. In this case the accelerations at the roller guide level becomes

$$\ddot{x}_l(t)=\left(\frac{a_l}{L}-1\right)\left(\ddot{U}_{n-1}-y_1\ddot{\Theta}_{n-1}\right)+\left(2-\frac{a_l}{L}\right)\left(\ddot{U}_{n-2}-y_1\ddot{\Theta}_{n-2}\right) \tag{2.54}$$

$$\ddot{y}_{l1}(t)=\left(\frac{a_l}{L}-1\right)\left(\ddot{V}_{n-1}+x_1\ddot{\Theta}_{n-1}\right)+\left(2-\frac{a_l}{L}\right)\left(\ddot{V}_{n-2}+x_1\ddot{\Theta}_{n-2}\right) \tag{2.55}$$

$$\ddot{y}_{l2}(t)=\left(\frac{a_l}{L}-1\right)\left(\ddot{V}_{n-1}+x_2\ddot{\Theta}_{n-1}\right)+\left(2-\frac{a_l}{L}\right)\left(\ddot{V}_{n-2}+x_2\ddot{\Theta}_{n-2}\right) \tag{2.56}$$

where $a_l = a_u + l_c$.

Finally, the input acceleration terms in (2.17) and (2.33) can be obtained from

$$\ddot{x}_c(t) = \ddot{x}_l + \frac{l_m}{l_c}(\ddot{x}_u - \ddot{x}_l) \tag{2.57}$$

$$\ddot{x}_e(t) = \frac{l_m}{l_c}(\ddot{x}_u - \ddot{x}_l) \tag{2.58}$$

$$\ddot{y}_c(t) = \frac{l_m}{2l_c}\left[\ddot{y}_{u1} + \ddot{y}_{u2} + \left(\frac{l_c}{l_m} - 1\right)(\ddot{y}_{l1} + \ddot{y}_{l2})\right] \tag{2.59}$$

$$\ddot{y}_e(t) = \frac{l_m}{l_c}(\ddot{y}_{l1} - \ddot{y}_{u1}) \tag{2.60}$$

$$\ddot{y}_e'(t) = \frac{1}{2}(\ddot{y}_{u1} - \ddot{y}_{u2}) \tag{2.61}$$

2.3 Numerical Results

Physical Properties of the System

A typical 4300-lb counterweight located in a 10-story torsional building is used in the analysis. The building is a slight modification from the building described by Conner et al. (1987). The building has a rectangular plan with a small eccentricity. As mentioned earlier, each floor of the building has two translational and one rotational degree-of-freedoms. The mass and stiffness properties of the building are shown in Table 2.1. The natural frequencies and mass matrix normalized participation factors are presented in Table 2.2. The building is assumed to have 5% modal damping ratio for all modes.

The 18.5-lb guide rail with no intermediate tie brackets is used as the basic system in the numerical analysis. The cross-sectional properties of this guide rail are shown in Table 2.3 along with other sizes provided by the code. The bracket supports are located on each floor level with 12 ft story height. The dimensions of the counterweight are height l_c = 138 in.,

width d = 28 in., and depth e = 6 in. The helical springs in the roller guide assemblies are made of steel with five coils having mean radius of 0.5 in and wire diameter of 0.25 in. The clearances between the restraining plates and the rail and between the frame and the rail are set to the maximum allowed by the code. An inherent modal damping ratio of 2% is assumed for all modes.

Seismic Inputs

Six sets of recorded ground accelerations, listed in Table 2.4, are used to excite the building to provide seismic input to the rail-counterweight system. Each set of accelerogram consists of two horizontal components in the perpendicular directions. In addition, a set artificial accelerogram corresponding to broadband Kanai-Tajimi spectral density function are also used as input to the building. For each intensity level, 50 sets of accelerograms are generated for this purpose. The average and mean plus one standard deviation pseudo-acceleration spectra of the sets with 0.1g maximum ground acceleration are shown in Figure 2.7.

The spectral density is in the form of

$$\Phi(\omega) = S \frac{\omega_g^4 + 4\,\beta_g^2\,\omega_g^2\,\omega^2}{(\omega_g^2 - \omega^2)^2 + 4\,\beta_g^2\,\omega_g^2\,\omega^2}$$

with parameters ω_g = 23.96 rad/s and β_g = 0.32. The synthetic ground acceleration $f(t)$ is generated as the sum of k harmonic functions with frequencies ω_k and random phase angles δ_k,

$$f(t) = \kappa(t)\sqrt{4\,\Delta\omega}\,\mathrm{Re}\left\{\sum_k \left[\sqrt{\Phi(\omega_k)}\,e^{i\delta_k}\right] e^{i\omega_k t}\right\}$$

where $\kappa(t)$ is a deterministic envelope function:

$$\kappa(t) = \begin{cases} (t/3)^2 & 0 \text{ s} \le t \le 3 \text{ s} \\ 1 & 3 \text{ s} \le t \le 10 \text{ s} \\ e^{-0.26(t-10)} & t > 10 \text{ s} \end{cases}$$

Seismic Response

A unique characteristic of the rail-counterweight system is that the frequency of the system change not only because of the contacts but also with different location of the counterweight along the rail. Figure 2.8 shows the natural frequencies of the system as a function of counterweight position along the building height. The frequencies shown are for the original system without any contacts between counterweight and the rail. If contact happens, the frequencies become much higher. For example, when the counterweight is at the top of the building, the first natural frequencies of the in-plane motion increases from 12.3 rad/s to 23.7 rad/s if contact happens at the lower roller guide assembly.

Figure 2.9 shows the time history of the in-plane displacement of the lower part of the counterweight under the actual El Centro ground motion. There are several occasions that the displacement exceeds the gap between the restraining plate and the rail, which is represented by the dashed line on the figure. It is also quite obvious that the frequency of the oscillation increases when this gap closed. The contact happens only for a short period of time. This requires the time step integration to be small enough to capture it. The fourth order Runge-Kutta method with adaptive time step was used in this analysis for its numerical efficiency and accuracy. For the sake of completeness, a numerical side-study performed in this connection is described in Appendix A.

Figures 2.10 and 2.11 show the maximum stresses in the rail and brackets for different counterweight positions along the building height. The maximum acceleration of the building floor under Northridge and El Centro earthquakes with maximum ground acceleration normalized to 0.1g are also plotted in the same figures. In both cases, the building actually amplifies the maximum acceleration of the ground motion and the highest acceleration occurs at the top of the building. However, the maximum stress in the rail or bracket does not necessarily happen when the counterweight is located at the top of the building.

The maximum stress in the web of the rail is higher than the maximum stress in the flange in both figures, indicating that the effect of the in-plane motion is more dominant than the out-of-plane. The patterns of maximum stresses are qualitatively similar for counterweight at different span of the rail. The stress in the bracket is higher when the lower roller guides are located close to the bracket support while the stress in the rail is higher when the counterweight is about at the middle of the rail span.

Parametric Study

The effects of several parameters of the rail-counterweight system are studied by conducting a parametric study. Since the trends of stress and force responses at different span of the rail are similar, the parametric study compares only the responses when the counterweight is located on the top story. First we look at the effect of the clearances required by the code, both between the restraining plate and the rail and between the frame and the rail. Other parameters are the size of guide rail, different ground motions and their intensities, and the use of intermediate tie-brackets.

Clearance at the Restraining Plate: Figures 2.12 and 2.13 show the maximum stresses in the rail and force in the brackets, respectively, for different clearances between the restraining

plate and the rail. Results under 0.1 g Northridge and El Centro earthquakes are both presented in the figures. The code limits this clearance to be no more than 3/16 of an inch, as indicated by the dashed line in the figures. From this limit, it is clear that the maximum stress and force increase if the gap is widened up to an optimal point, and then decrease until the gap is wide enough that there are no contacts. On the other hand, reducing the gap size seems to improve the responses. However, this also means more contact and probably more impact noise during the earthquake.

Clearance Between the Frame and Rails: The effect of clearance between the frame and the rail is presented in figures 2.14 to 2.16. The code requires that this clearance to be 0.5 inch or less in order to limit the rail deformation in the in-plane direction when the counterweight is located on two consecutive spans. If the deformation of the rail closes the gap, part of the force will then be transferred directly to the support. The results shown in Figures 2.14 to 2.16 are obtained with actual Northridge (0.843g) and El Centro (0.348g) earthquakes because the low intensity of 0.1g considered earlier did not produce any contact between the rail and the frame.

Figure 2.14 shows that the maximum stress in the rail can be reduced significantly, especially for Northridge case, if the clearance is reduced. There are no significant effects on the maximum stress under El Centro earthquake, but the maximum stress in this case is already low. Figure 2.15 shows similar plot for the maximum in-plane force in the bracket. The maximum in-plane force seems to increase with decreasing clearance for El Centro earthquake but this is not always the case for the Northridge earthquake. This maximum in-plane force under Northridge earthquake is then plotted in Figure 2.16 as a function of counterweight location on the top story of the building for different values of clearances. This

figure shows that for small clearance, the contacts occur at a large range of counterweight position in the middle of rail span. For larger clearance, the range is more confined to the counterweight location near the middle of the span. However, this figure indicates that larger range of contact does not necessarily produce higher force in the bracket.

Effect of Rail Size: The next set of figures present the response of the rail-counterweight system for different rail sizes, 12-lb, 18.5-lb, and 30-lb. The maximum stress in the rail under actual Northridge and El Centro earthquakes are plotted respectively in Figures 2.17 and 2.18, while Figure 2.19 shows the maximum in-plane force under actual Northridge earthquake. As expected, larger rails experience smaller maximum stress. In addition, smaller rails have larger deformation that creates wider range of contact in the middle of the span, as shown in Figure 2.19, and thus produces higher in-plane force in the bracket. It should be noted that according to the code all the three sizes are acceptable for the 12 ft. support spacing without intermediate tie-bracket that is used in this study. However, Figure 2.17 shows that even the 18.5-lb. rail is not sufficient for actual Northridge earthquake.

Effect of Different Seismic Inputs: Figures 2.20 to 2.26 show the effects of different ground motions and different intensities to the responses of the rail-counterweight system. The six earthquake records mentioned in table 1 are used as the base motion to the building. In Figure 2.20, the maximum stresses in the rail under the actual earthquakes, which of course have different intensities. This figure shows that the stress under Northridge earthquakes is the highest although the maximum ground acceleration of the earthquake is not the highest. In Figure 2.21, all earthquakes are normalized to 0.5g. Again, Northridge earthquake produces the highest stress in the rail. The effect of actual El Centro is below average of the actual earthquakes but it becomes close to the effect of Northridge when all earthquakes are

normalized to 0.5g. Similar observation can be obtained from figure 2.22 for the in-plane force in the bracket. The normalized Northridge earthquake gives the highest force followed closely by El Centro. Figures 2.23 to 2.25 show the average, maximum, and minimum values of the stresses and forces in Figures 2.20 to 2.23. Comparing Figures 2.23 and 2.24, it can be seen that normalizing the earthquake inputs to the same maximum ground acceleration will narrow the range of the maximum stress in the rail. Finally, in Figure 2.26 the maximum stresses in the rail are plotted for increasing maximum ground acceleration of the six earthquake records. This figure show that a moderate Northridge or strong El Centro earthquakes make the rail overstressed above the allowable stress while other earthquakes do not have that effect. These point to the need of considering several ground motions that are representative to the site of the building in evaluating the performance of the rail-counterweight system of an elevator.

Effect of Tie-Brackets: Figures 2.27 to 2.30 show the effect of installation of intermediate tie-bracket to connect the mid-span of the rail. According to the code, larger spacing of brackets is allowed if the tie-brackets are installed to tie the rails. In this study the tie-brackets are added to the original system without changing the bracket spacing. Figures 2.27 and 2.28 show that the intermediate tie-bracket can reduce the maximum stress in the rail when the counterweight is located at the middle of the rail span. It also reduces the contact between the frame and the rail, and thus reducing the force due to this contact, as shown in Figures 2.29 and 2.30. However, all these figures also show that the stress and force when the counterweight is at other locations, especially near the bracket support, could increase. In fact, for low intensity of Northridge (0.1g) the stress in the rail with tie-bracket is higher than the original system.

Fragility Study

Up to this point, the responses of the rail-counterweight have been obtained with several recorded ground motions from different events at different locations. The next set of results presents the statistics of the responses under an ensemble of ground accelerations having similar frequency characteristics as mentioned earlier in this section. Besides comparing the mean values or mean plus one standard deviation values of the responses to their maximum allowable values, the results can also be presented in terms of fragility of the rail-counterweight system.

Fragility of a system or its component is defined as the conditional probability of failure for a given value of seismic intensity parameter such as peak ground acceleration. It provides an important piece of information needed for seismic risk analysis of structural or mechanical systems (Kennedy and Ravindra, 1984). For the rail-counterweight system considered in this study, the failure is defined in terms of the induced stress S in the rail or bracket exceeding the yield strength R of the material. For a given maximum ground acceleration y, the fragility expressed as the conditional probability of failure can be written as

$$F(y) = P\left[S \geq R \middle| Y = y \right] \tag{2.62}$$

To estimate this probability of failure, the probability distributions of R and S must be known. Here, it is assumed that R and S are lognormally distributed. For the yield strength R of the rail and bracket material, the mean value equal to 1.05 times the nominal value with the coefficient of variation of 0.1 is assumed (Brockenbrough, 1999). Similar parameters for the induced stress S are obtained by dynamic analysis of the rail counterweight system for the ensemble of ground acceleration mentioned above.

For each counterweight position along the rail, failure can happen at different locations of the rail. The probability of failure for a specific location of the counterweight, $P_{f\text{-}i}$, is determined by the largest of the probabilities of failure $P_{f\text{-}ij}$ of seven different points on each rail and six bracket locations affected by each counterweight position

$$P_{f-i} = \max_j P_{f-ij} \tag{2.63}$$

To obtain the probability of failure considering all counterweight positions, the probability of failure for each location of counterweight is then convoluted with the probability of counterweight being on that specific location. Assuming that the counterweight can be anywhere along the rail with equal probability, a uniform distribution for counterweight position is justified. With this the unconditional probability of failure of the system, considering all positions of the counterweight is equal to the average the probabilities of failure calculated at discrete locations along the height

$$P_f = \frac{1}{N}\sum_i P_{f-i} \tag{2.64}$$

where N is the number of discrete locations where the probabilities of failure were calculated.

Figure 2.31 shows the statistics of the peak rail stress under the ensemble of synthetic ground motions. Although the mean values are still below maximum allowable stress up to 1g, the mean plus one standard deviation and the absolute maximum values present the possibility of overstress in the rail. The figure also shows that the increase in the responses does not vary linearly with the increase of maximum ground acceleration. Figures 2.32 and 2.33 compare the responses of the system with and without intermediate tie-bracket. The tie-bracket seems to help in reducing the peak stress and the fragility of the rail especially for strong earthquakes.

2.4 Concluding Remarks

An analytical model of the rail-counterweight system has been developed incorporating the detail of the guiding and support system of the counterweight, and the system nonlinearities. Nonlinearity caused by closing and opening of the clearances at the restraining plates is included in the model by using equivalent springs with bilinear force-deformation relationship at the four corners of the counterweights. Similarly the nonlinearity caused by the on-off contact of the frame with the rails at the bracket supports is included through the use of a spring with another bilinear models added at the point of contact of the frame with the rails. Depending upon the position of the counterweight along the building height, the location of this spring on the frame would change. The model also includes the effect of differential support motion filtered through the building and applied at the bracket supports.

The analysis shows that although the building accelerations are usually heights in the top story, the maximum response in the counterweight-rail system does not necessarily occur there. The patterns of the variation of the maximum stress in different spans of the rails in different stories responses are similar. The stresses in the rails are higher when the top roller guide is at about the middle of the rail span, while the highest force in the bracket happens when the roller guide is on or near a bracket support.

The maximum stress in the rail and force in the bracket can be reduced by reducing the 3/16 inch gap specified by the code. However, this will cause more contact between the restraining plates and the rail and thus more impact noise during earthquake. Similarly, reducing the ½ inch gap between the frame and the rail can help reducing the maximum stress in the rail, especially under strong earthquakes. The reduction will create larger range of

contact between the frame and the rail, but this larger range does not necessarily mean higher force in the bracket.

The larger rail sizes, as expected, experience lower maximum stress and also have less contact with the counterweight frame. The installment of intermediate-tie bracket can also help in reducing the maximum stress in the rail, especially for strong earthquakes. However, there is possibility that the stress will increase when the counterweight is located near the support. This increase should be checked whether it would exceed the original maximum stress, thus nullifying the effect of the tie-bracket.

The variation in the responses due to different ground motions is quite large. This points to the need of considering an ensemble of site-specific ground motions to evaluate the performance of the rail-counterweight system. The range of variation can be slightly reduced if the maximum ground acceleration is normalized to a certain value. The maximum stress also increases with increasing intensity of the ground motion. This increase in the stress, however, does not relate linearly with the increase in the ground motion due to the nonlinearities in the system.

Fragility of the rail-counterweight system expressed as the conditional probability of failure of the rail, conditioned on the level of ground motion intensity, is also evaluated. In later chapters, such fragility analyses will be used to measure the effectiveness of different protective systems that are proposed for mitigating the seismic effects on the counterweight.

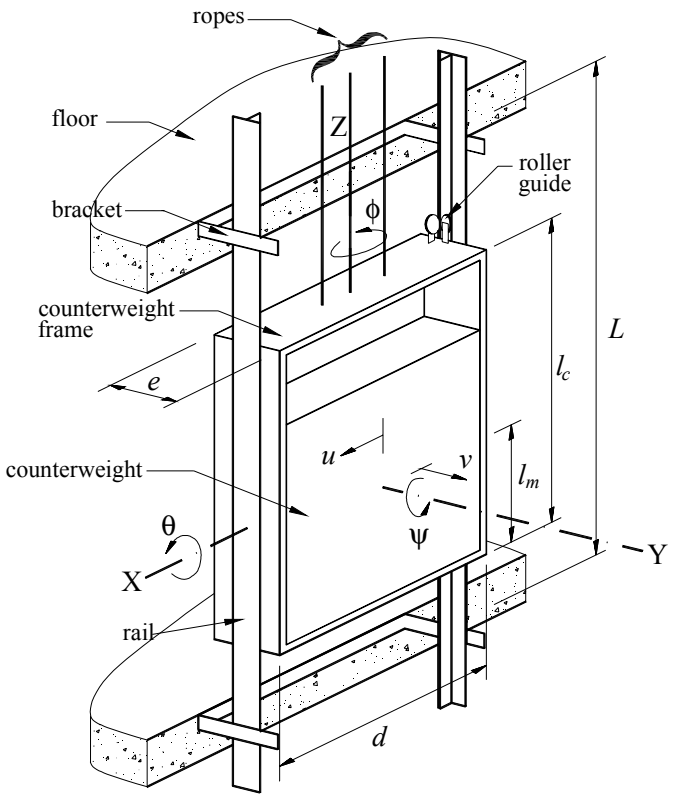

Figure 2.1 Geometry of the five degree-of-freedom model of the rail-counterweight system.

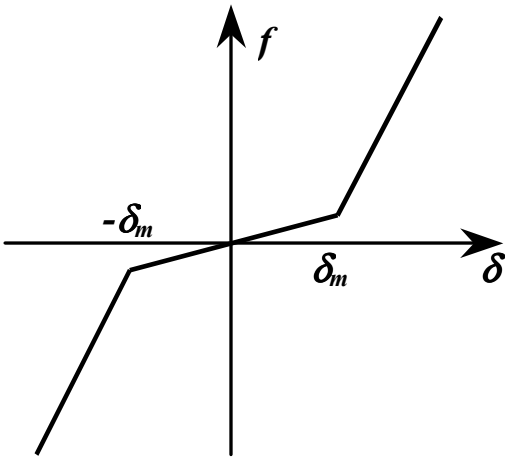

Figure 2.2 Bilinear force-deformation diagram due to contact between the restraining plate and the rail.

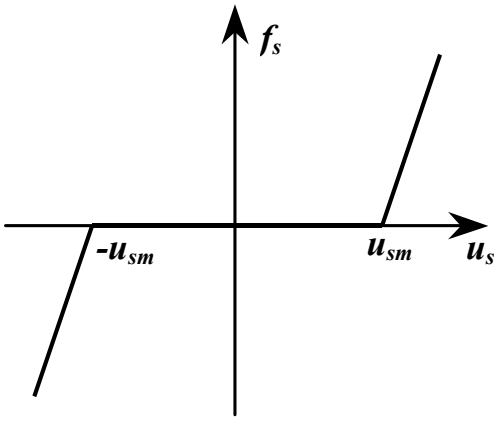

Figure 2.3 Bilinear force-deformation diagram due to contact between the counterweight frame and the rail.

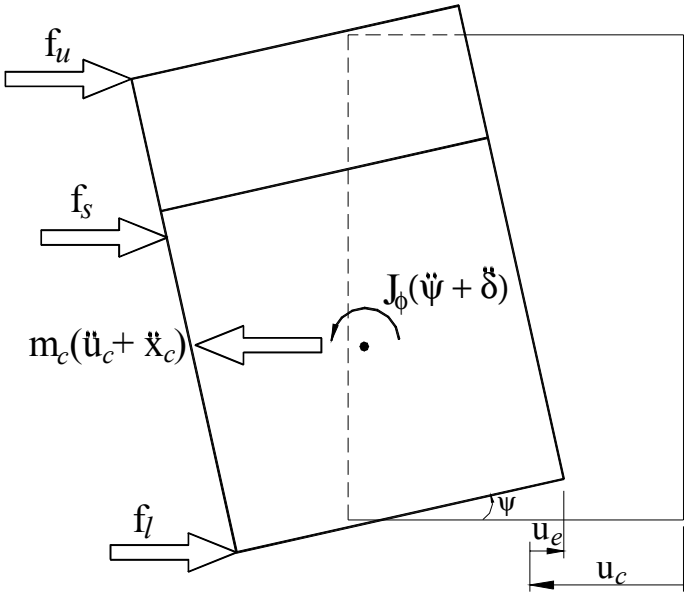

Figure 2.4 Free body and kinetic diagram for the in-plane motion of the counterweight.

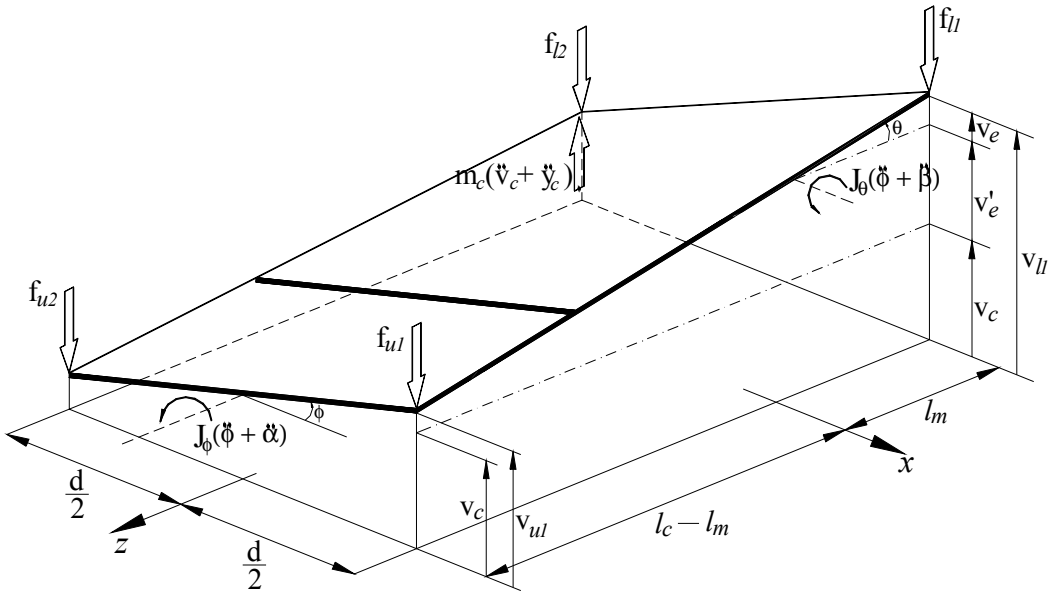

Figure 2.5 Free body and kinetic diagram for the out-of-plane motion of the counterweight.

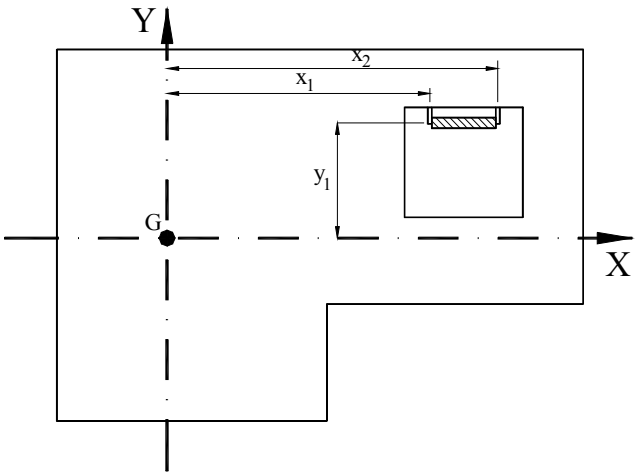

Figure 2.6 Location of the elevator hoistway on a typical floor plan.

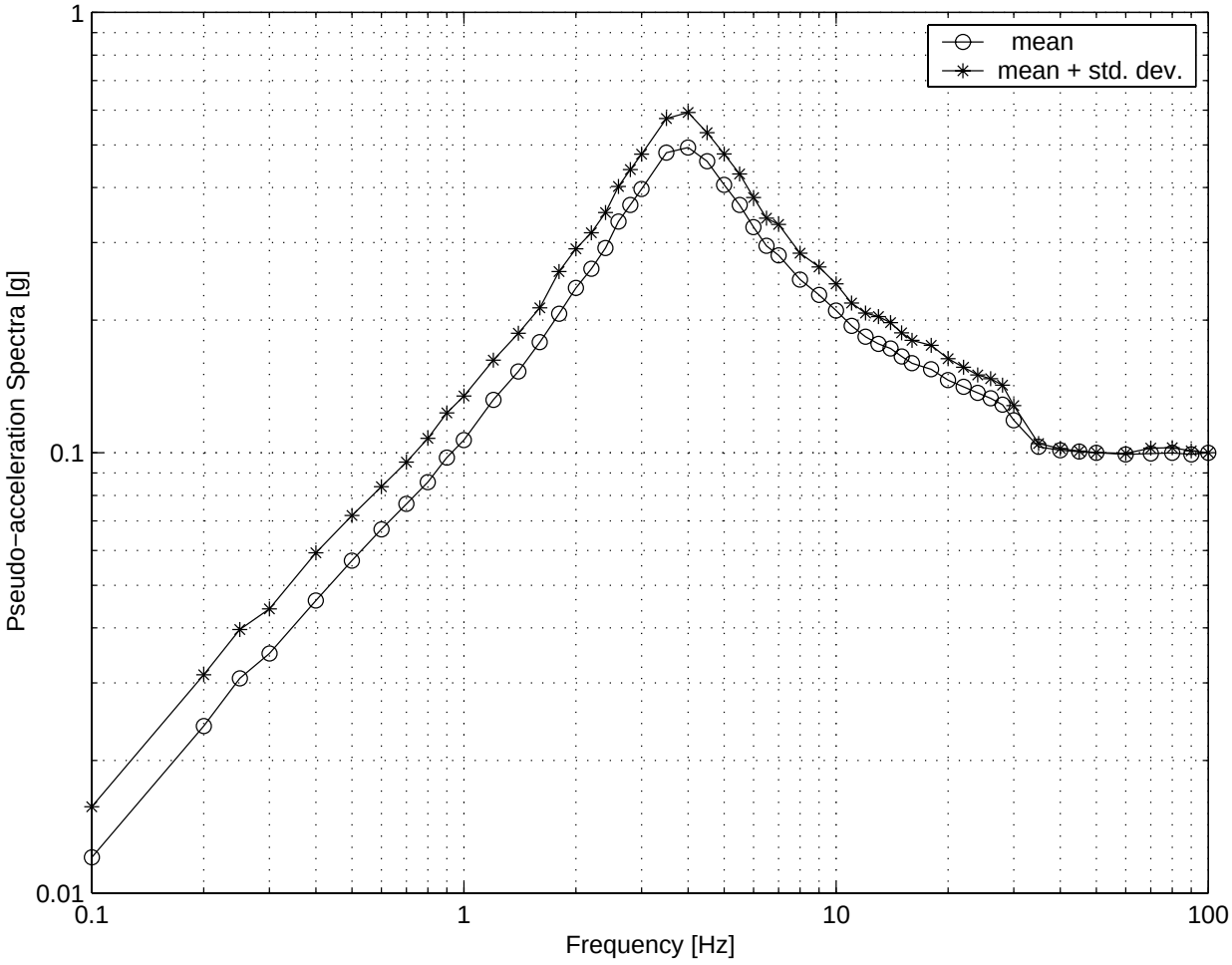

Figure 2.7 Mean and mean-plus-one-standard deviation of pseudo acceleration spectra of 50 sets of synthetic earthquakes with maximum ground acceleration of 0.1g

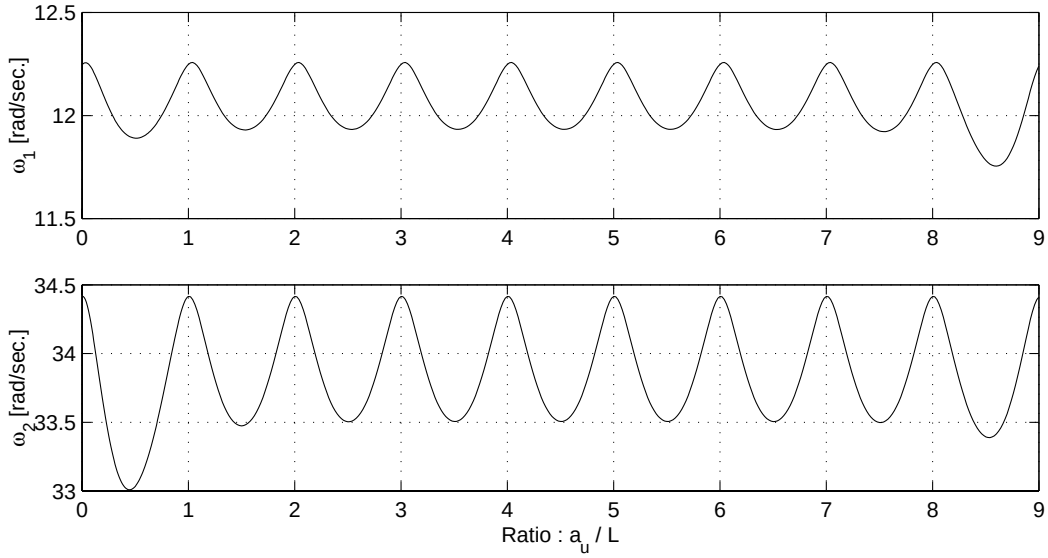

(a) In-plane motion

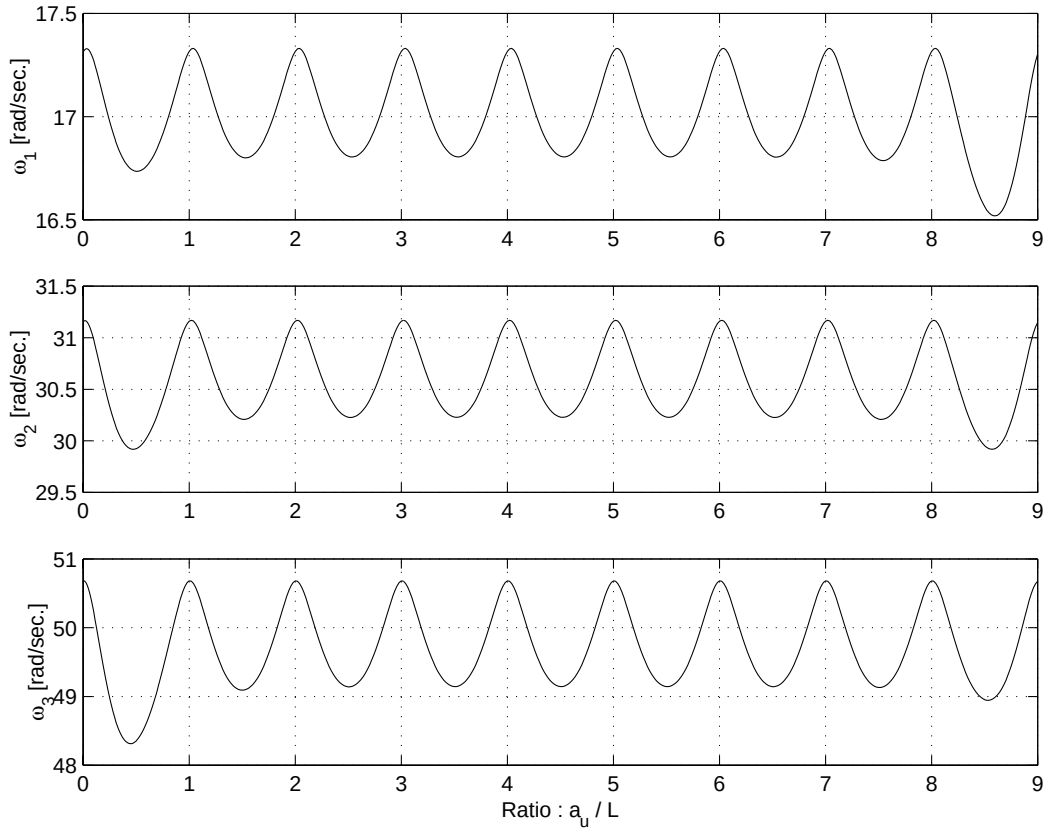

(b) Out-of-plane motion

Figure 2.8 Natural frequencies of the system for different counterweight positions along the 10-Story Building for 18.5-lb. rail

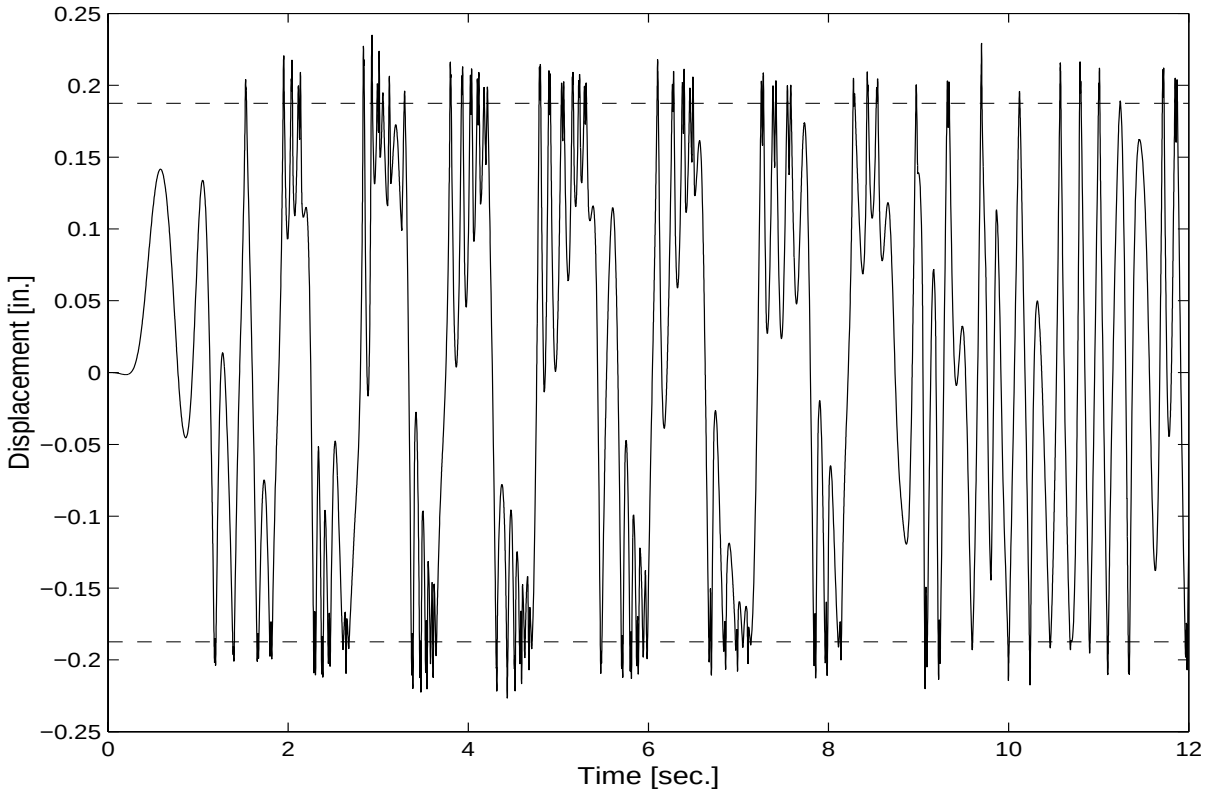

Figure 2.9 Time history of the in-plane displacement at the lower support of the counterweight

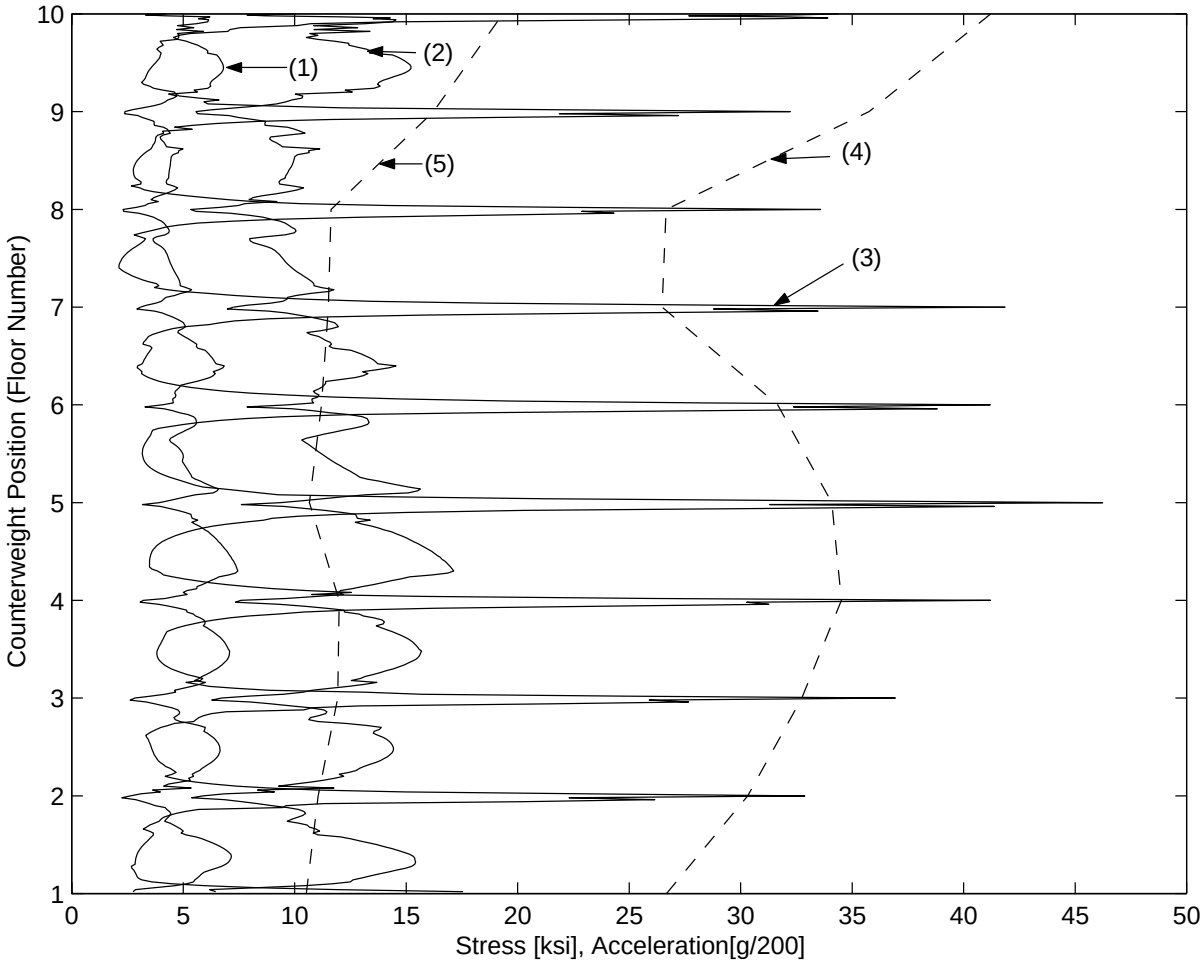

Figure 2.10 Maximum stress in the (1) rail flange, (2) rail web, and (3) brackets; and maximum floor acceleration in (4) the x-direction and (5) y-direction under Northridge earthquake 0.1g.

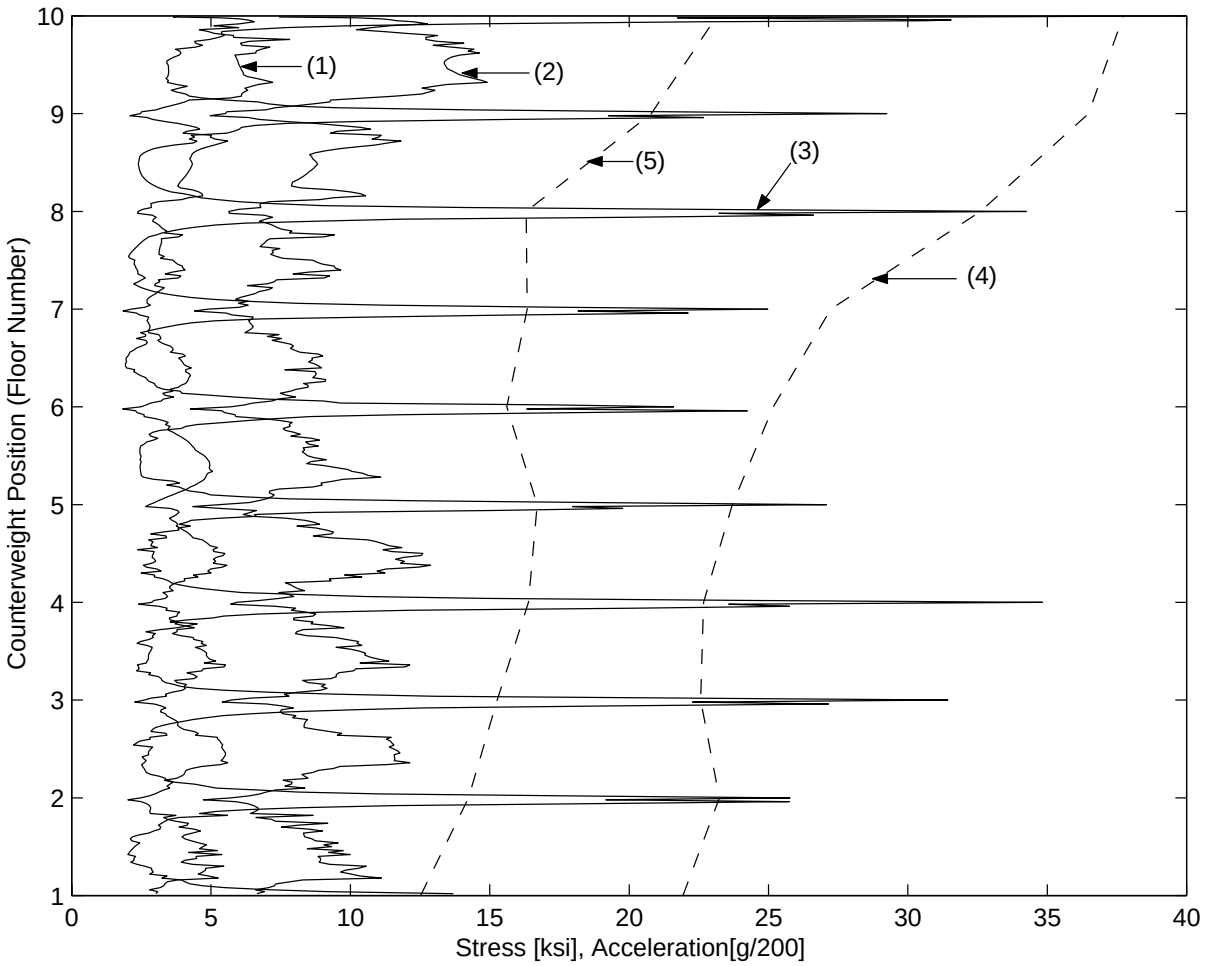

Figure 2.11 Maximum stress in the (1) rail flange, (2) rail web, and (3) brackets; and maximum floor acceleration in (4) the x-direction and (5) y-direction under El Centro earthquake 0.1g.

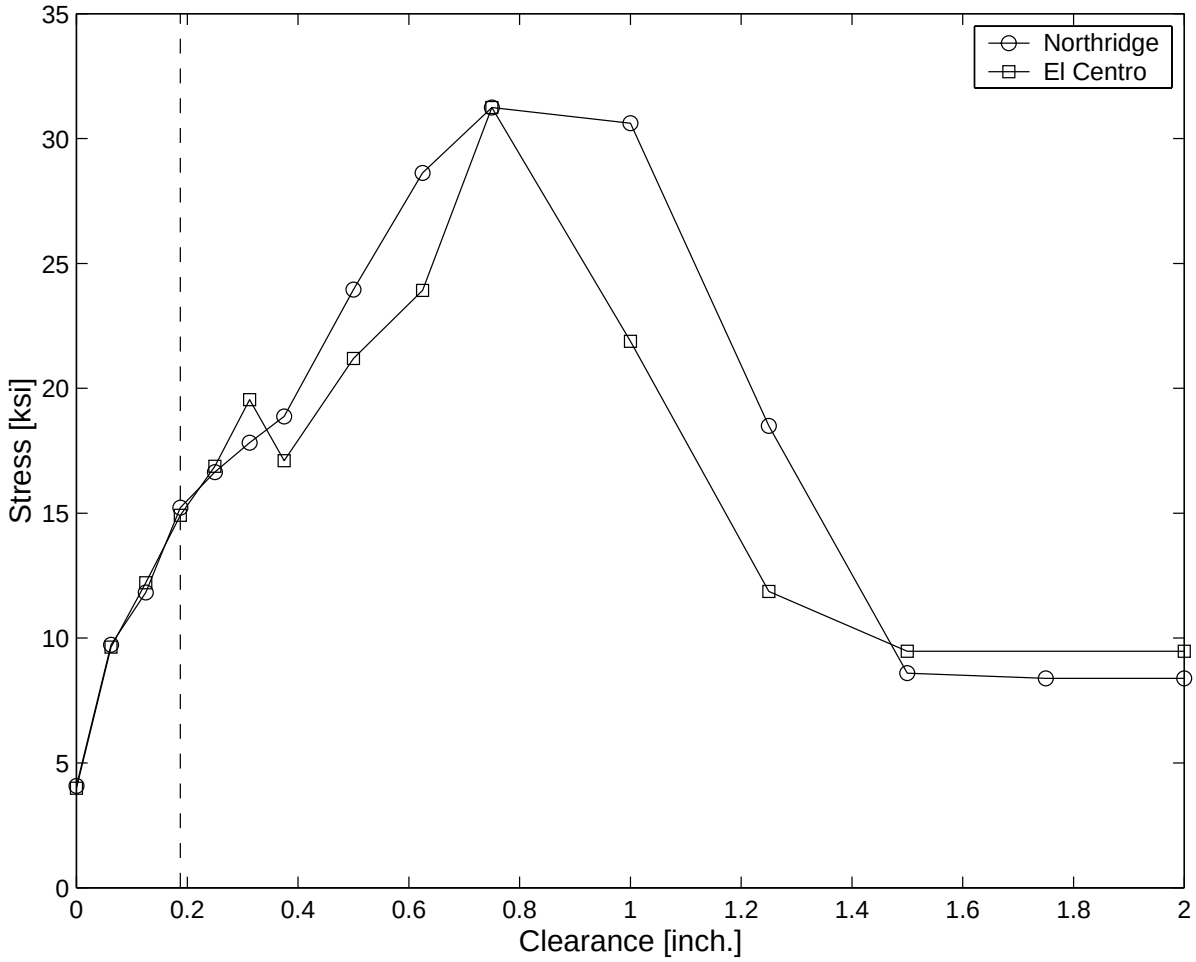

Figure 2.12 Maximum stress in the rail for different clearance at the restraining plate for 0.1g Northridge and El Centro earthquakes.

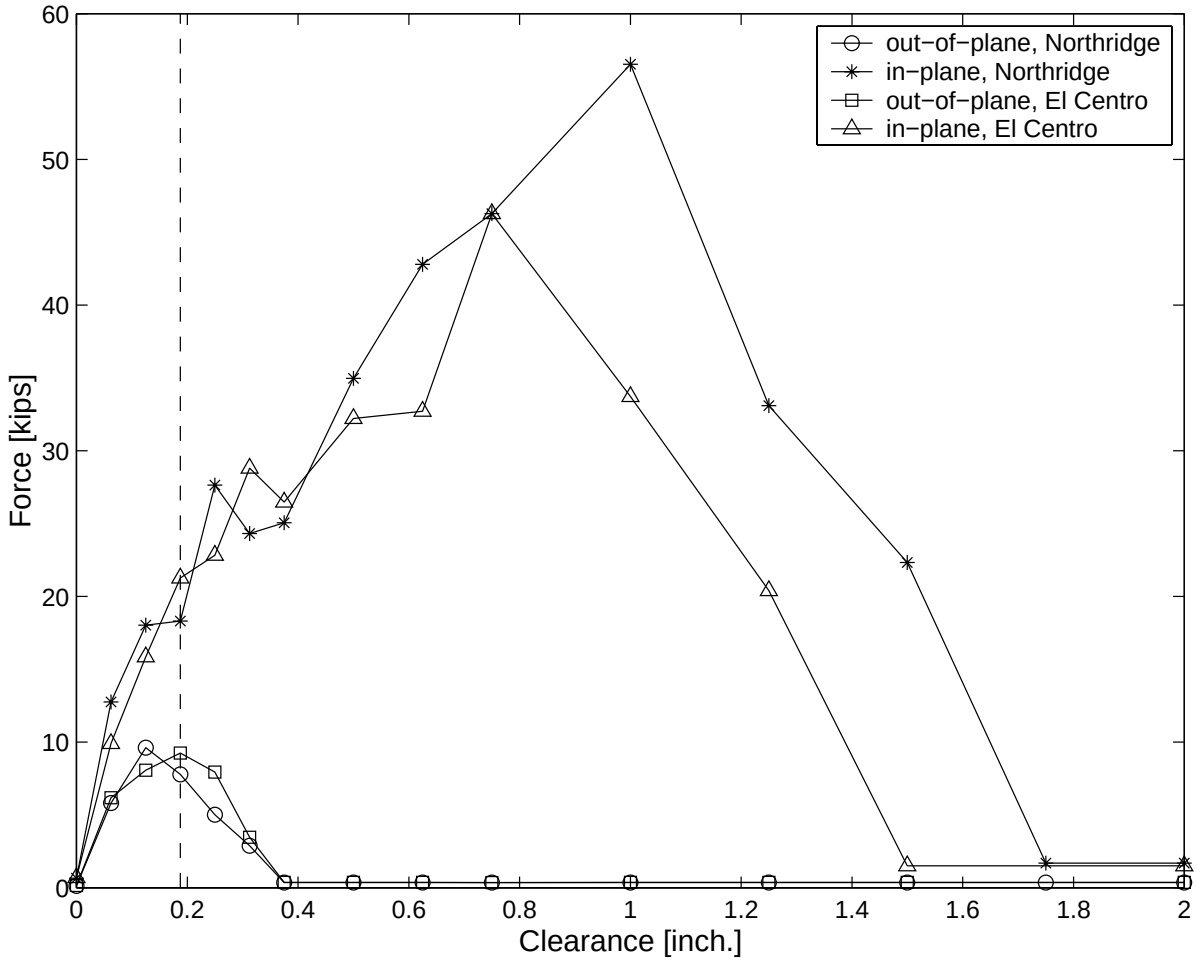

Figure 2.13 Maximum force in the bracket for different clearance at the restraining plate for 0.1g Northridge and El Centro earthquakes.

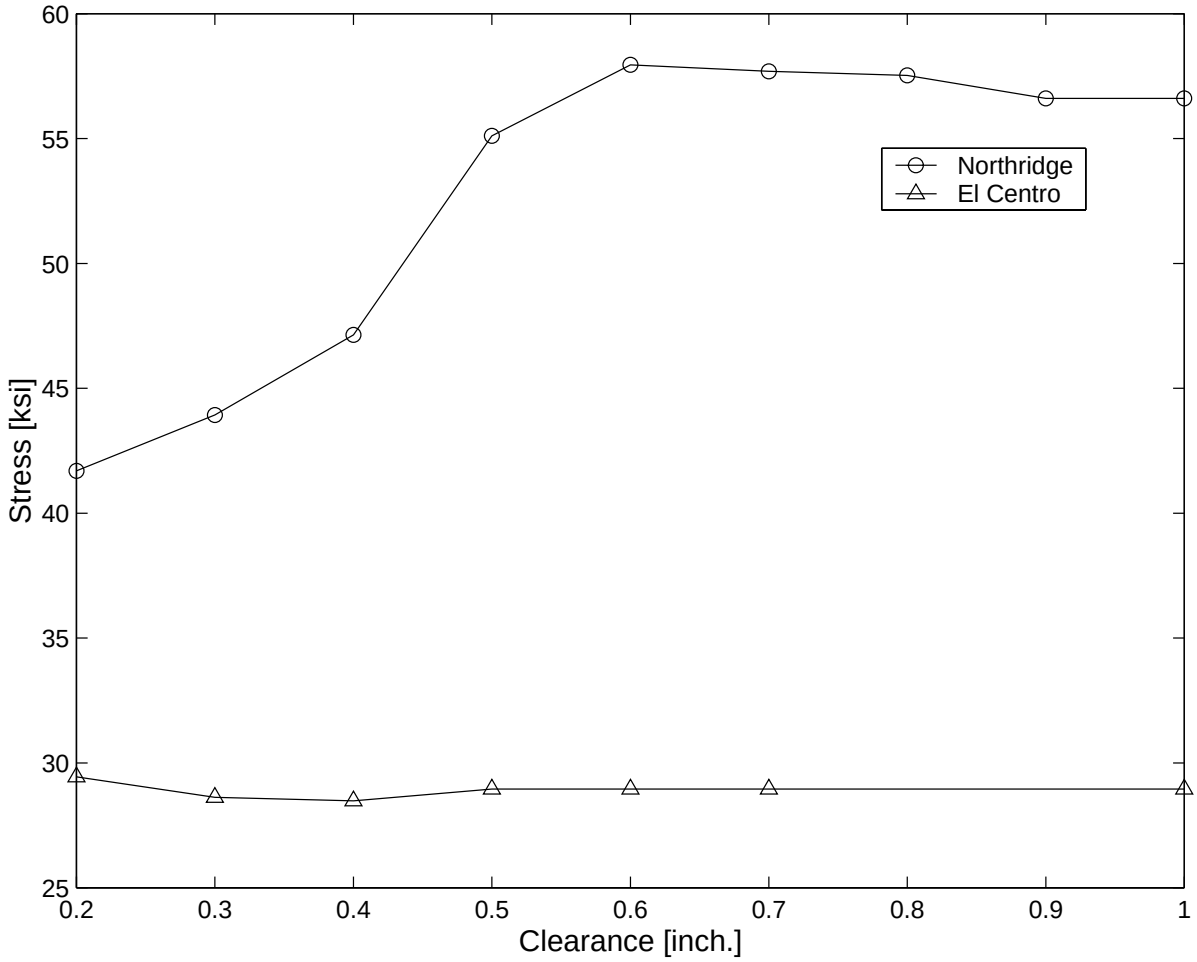

Figure 2.14 Maximum stress in the rail as a function of frame clearance for actual Northridge (0.843g) and El Centro (0.348g) earthquakes.

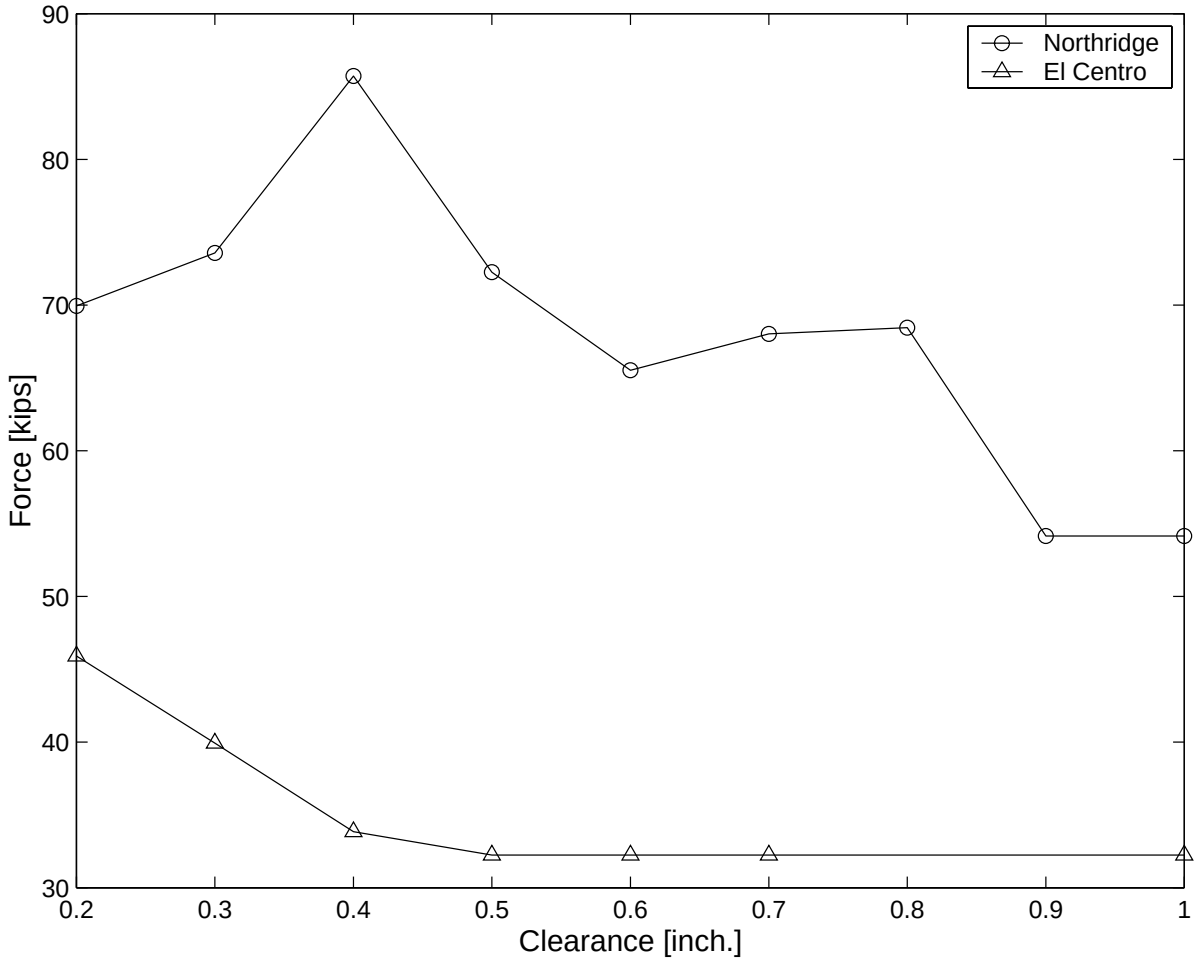

Figure 2.15 Maximum in-plane force in the bracket as a function of frame clearance for actual Northridge (0.843g) and El Centro (0.348g) earthquakes.

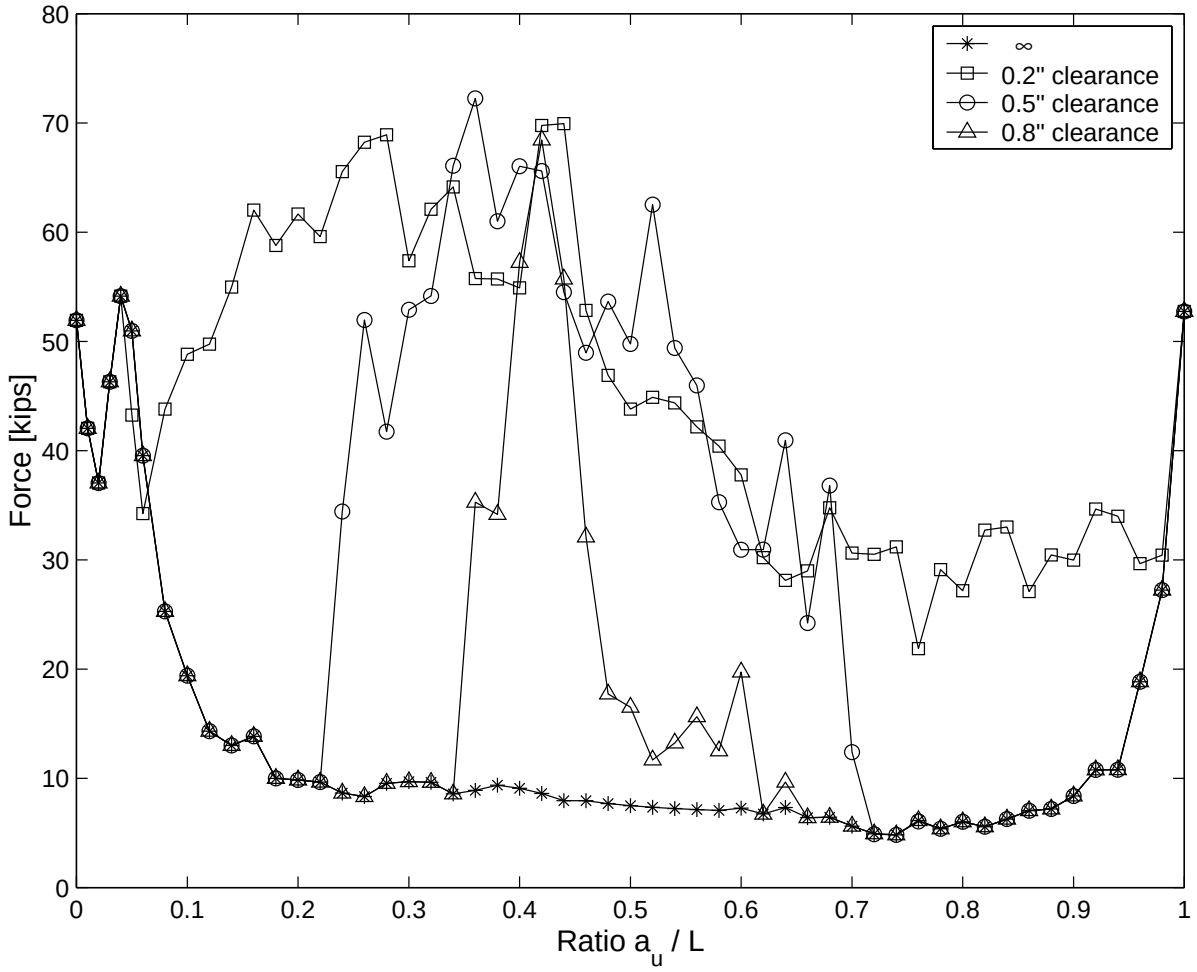

Figure 2.16 Maximum force in the bracket as a function of counterweight position on the top story for different frame clearance under actual Northridge (0.843g) earthquake.

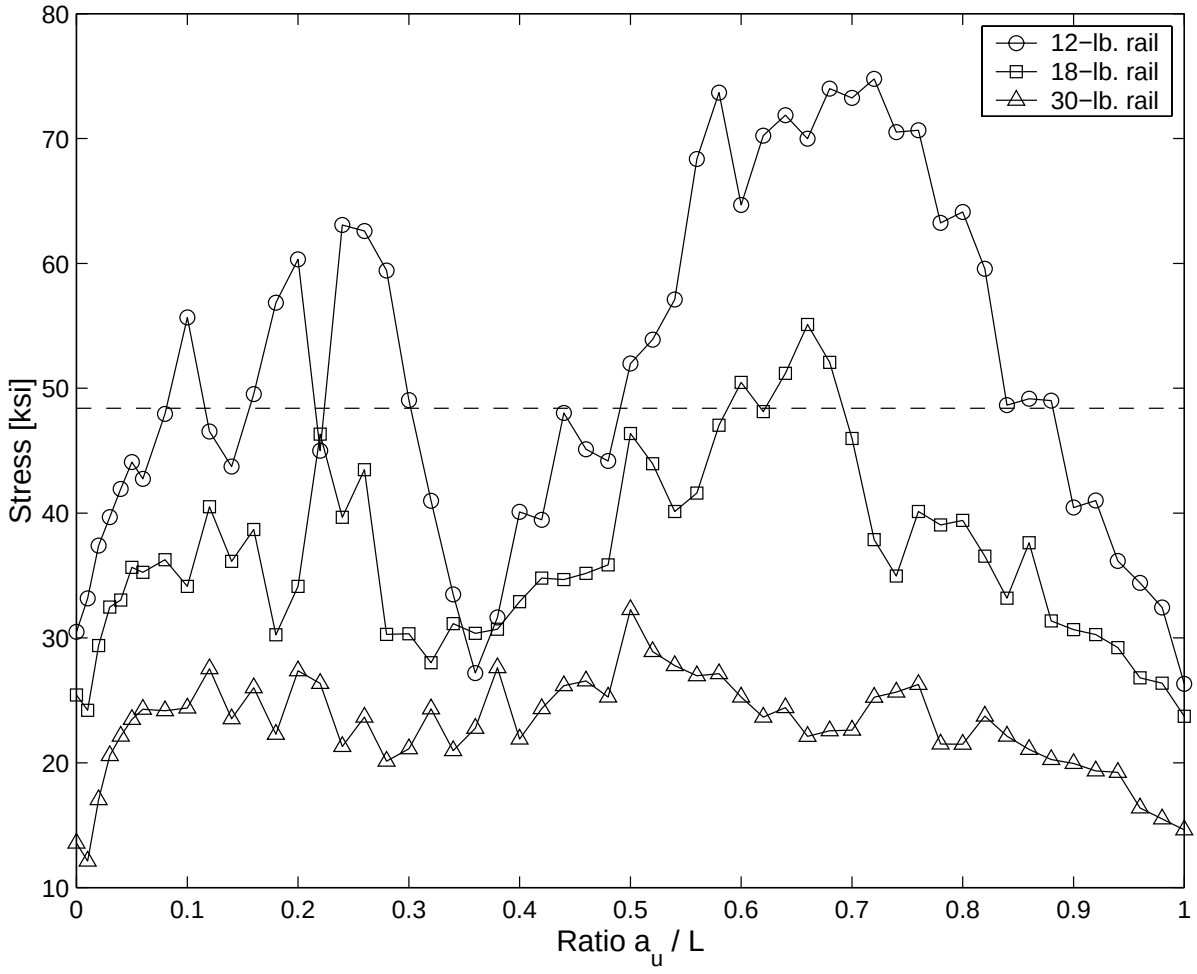

Figure 2.17 Maximum stress in different sizes of rail under actual Northridge earthquake (0.843g)

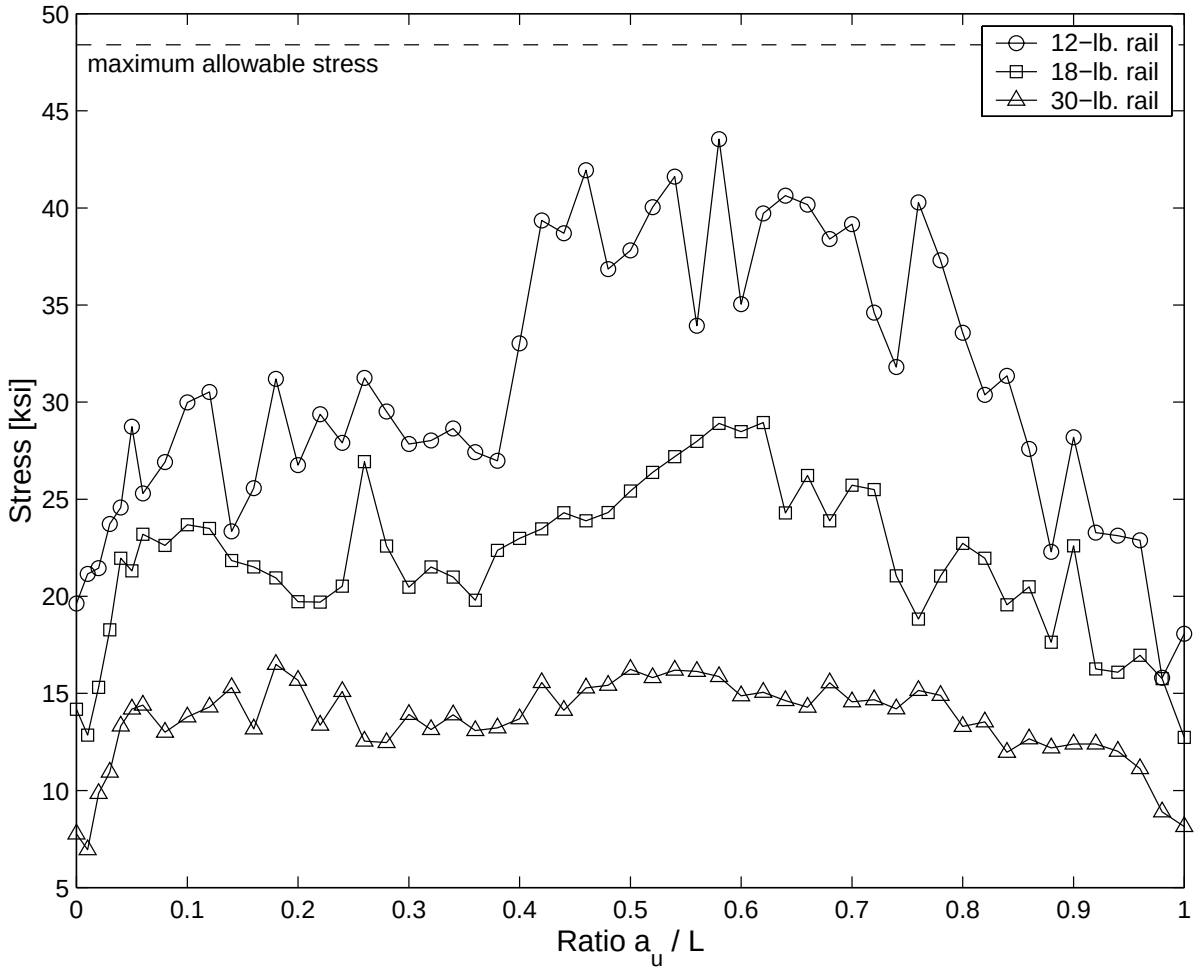

Figure 2.18 Maximum stress in different sizes of rail under actual El Centro earthquake (0.348g)

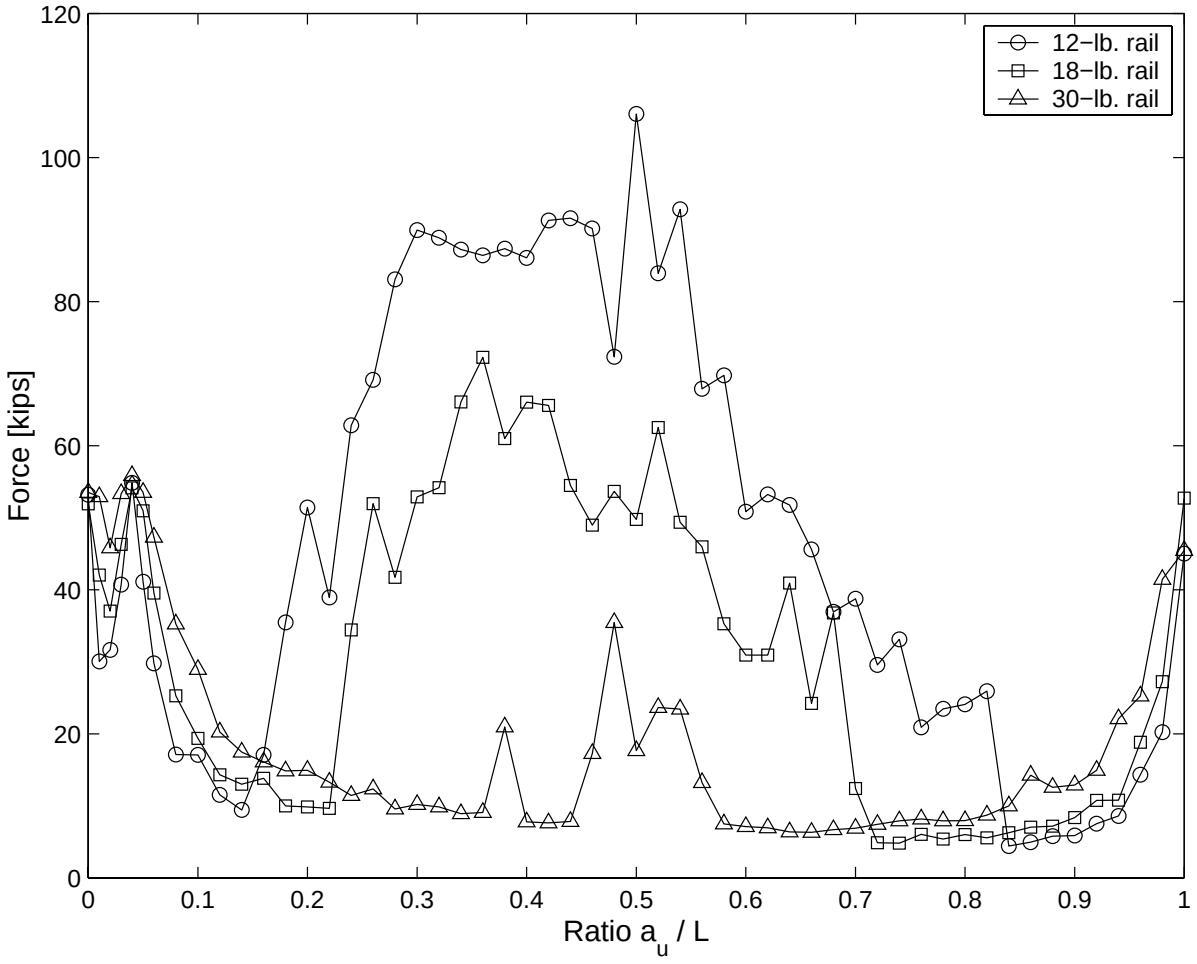

Figure 2.19 Maximum in-plane force in the bracket for different rail size, actual Northridge earthquake (0.843g).

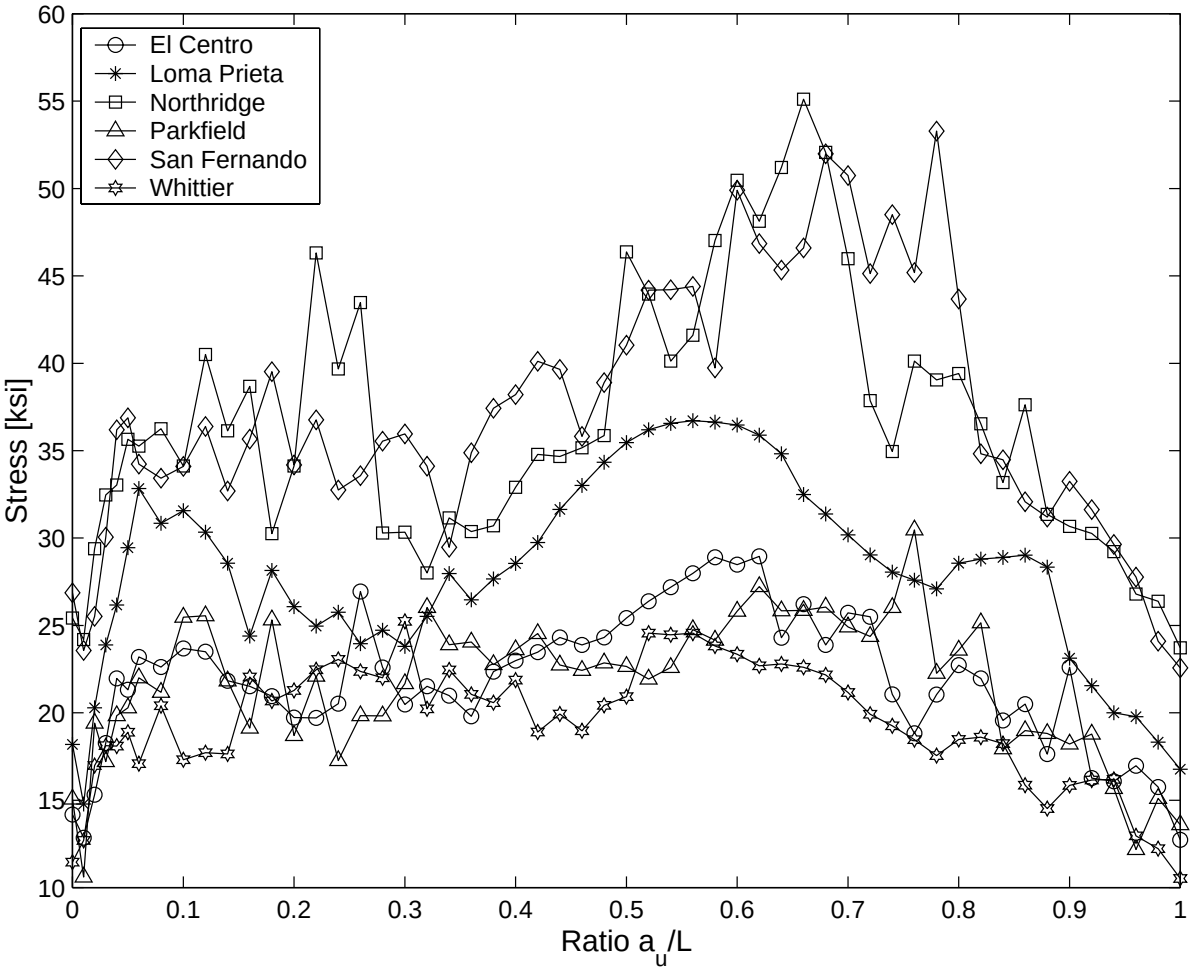

Figure 2.20 Maximum stress in the rail for different base inputs (actual as recorded ground motion)

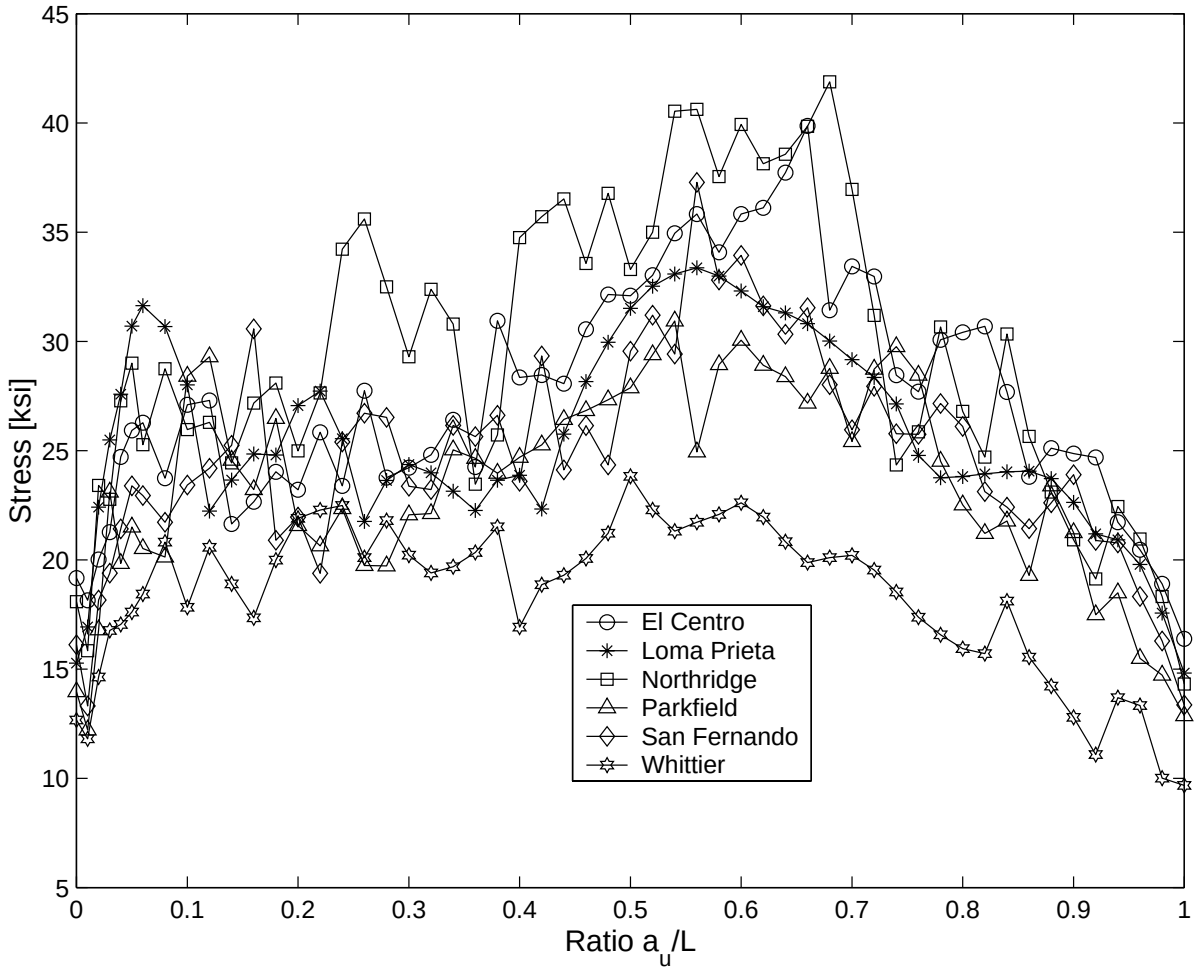

Figure 2.21 Maximum stress in the rail for different base inputs, all normalized to 0.5g.

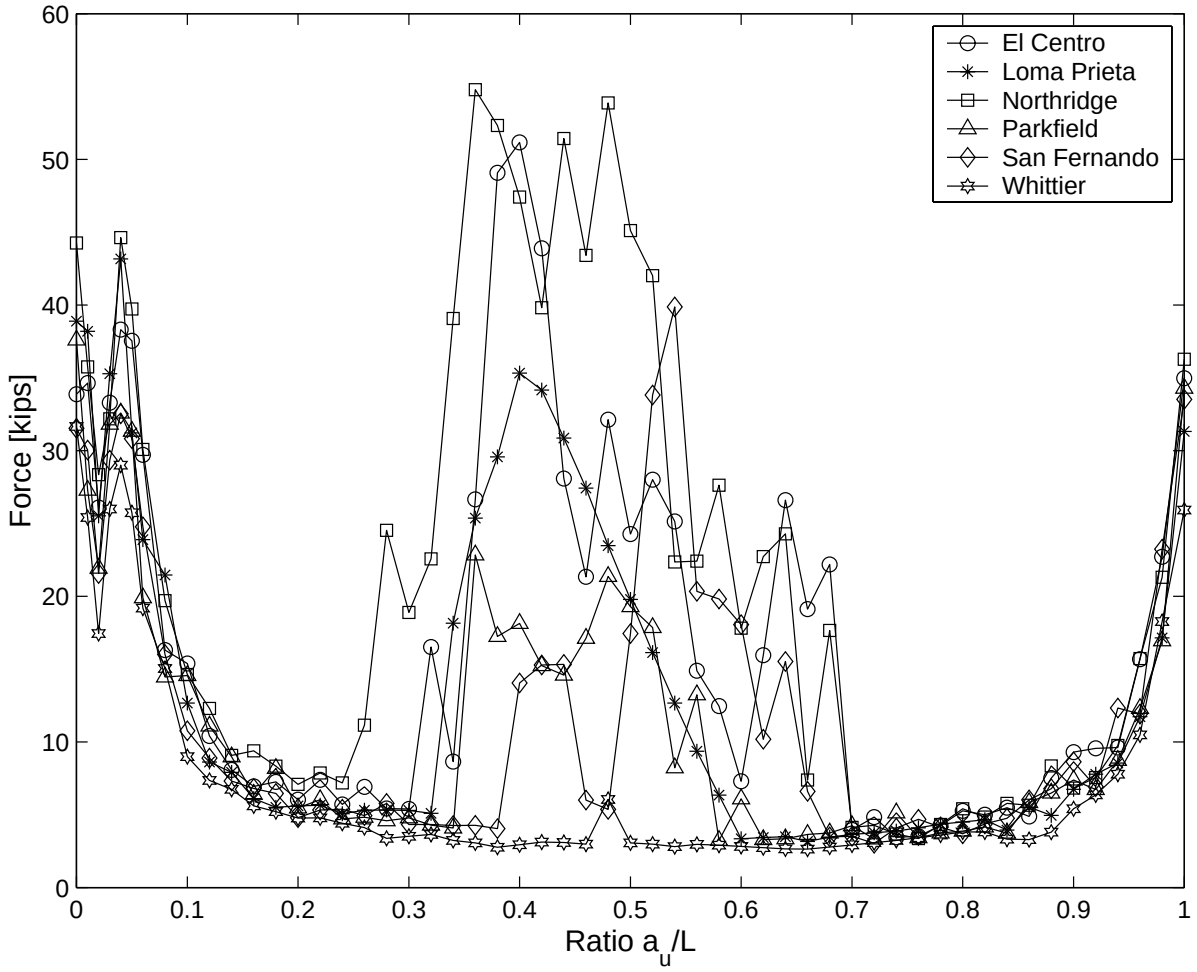

Figure 2.22 Maximum in-plane force in the bracket for different base inputs, all normalized to 0.5g.

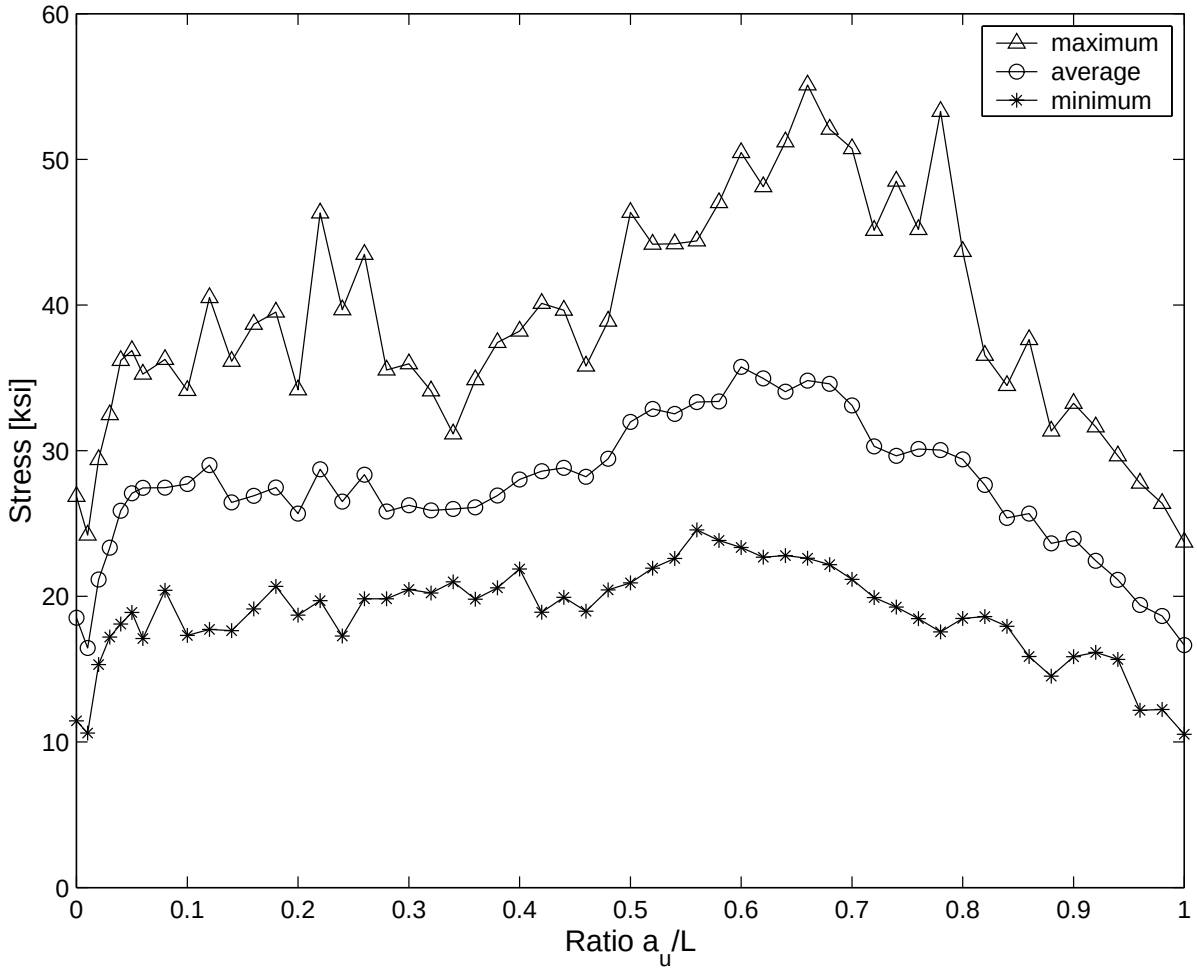

Figure 2.23 Average, maximum, and minimum values of the stress shown in figure 2.20.

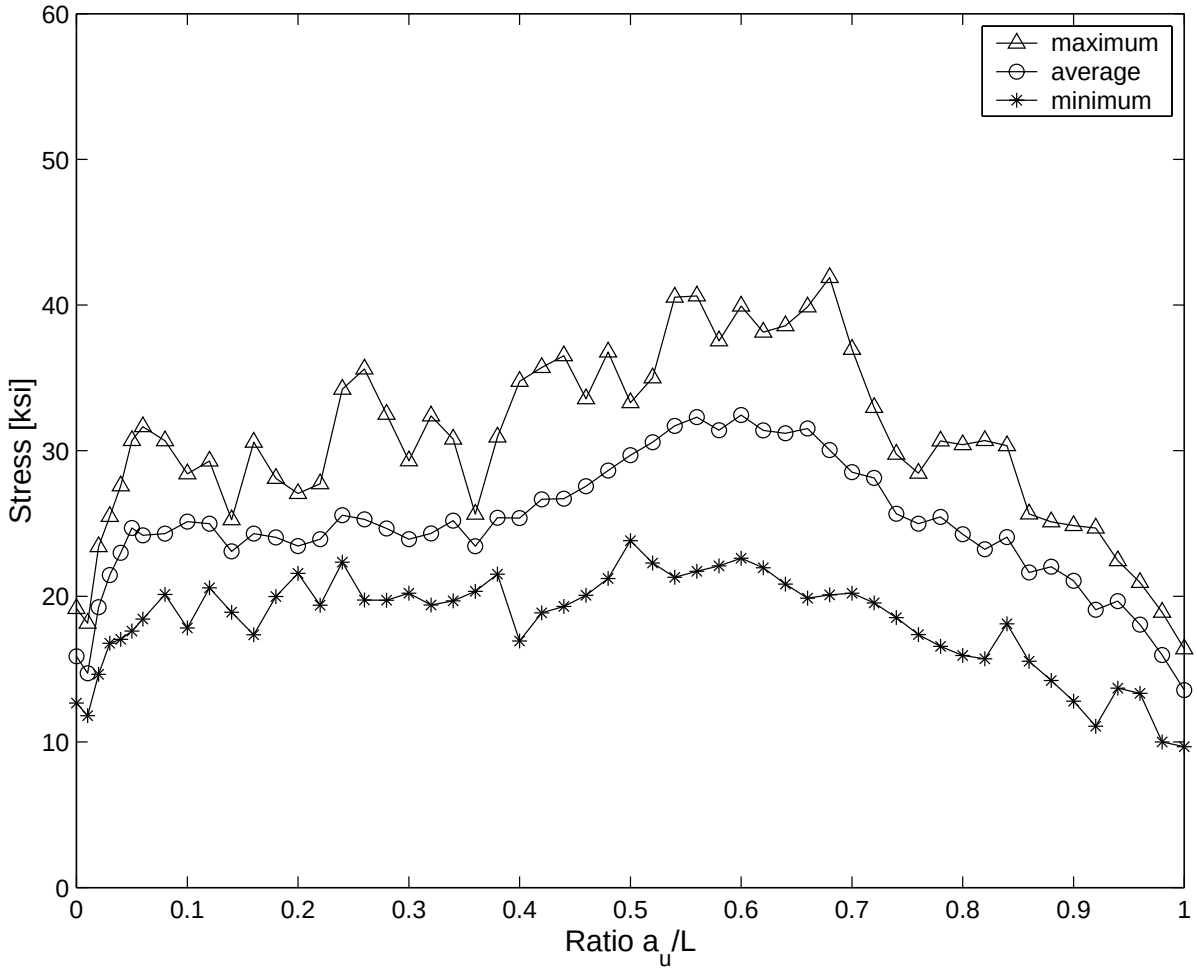

Figure 2.24 Average, maximum, and minimum values of the stress shown in figure 2.21.

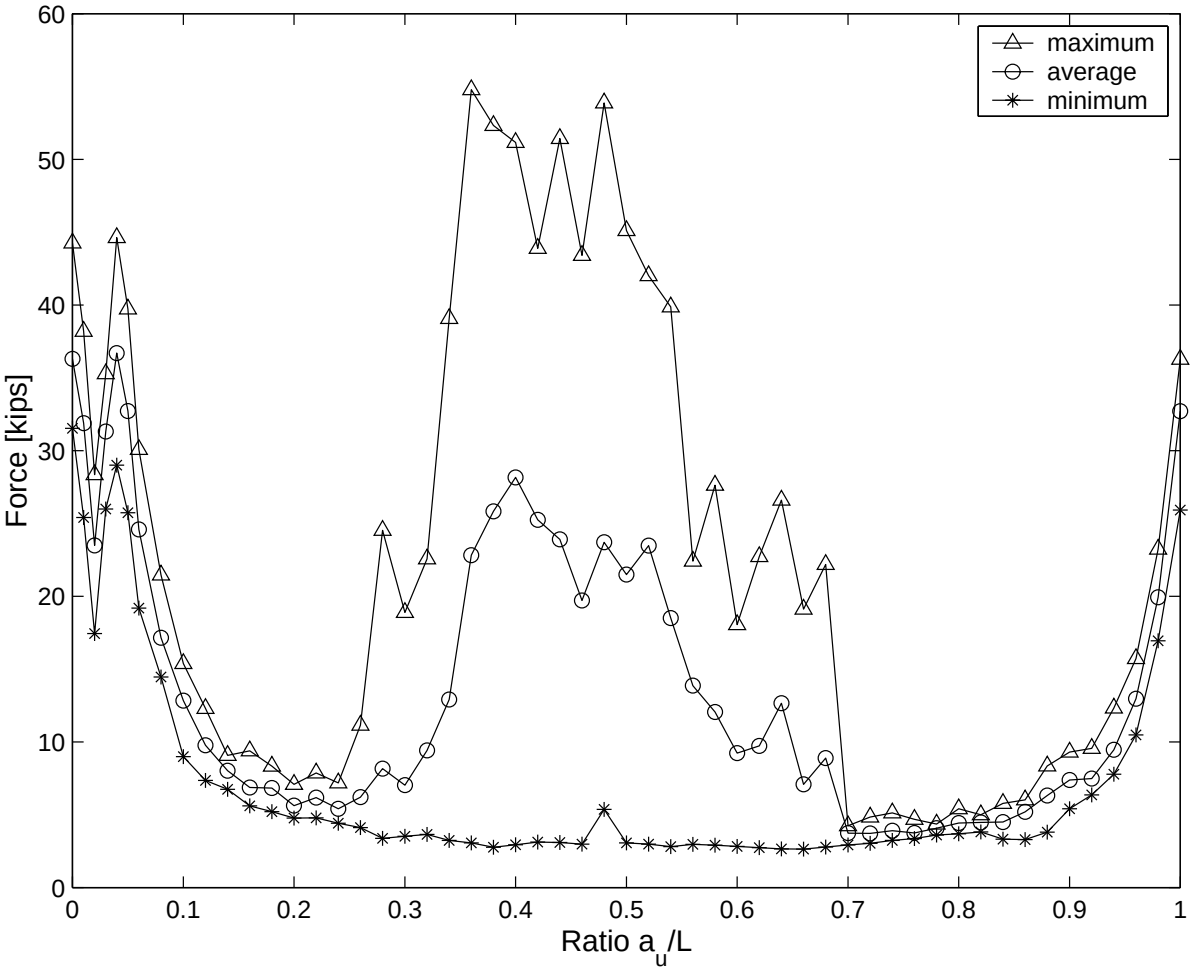

Figure 2.25 Average, maximum, and minimum values of the in-plane force shown in figure 2.22.

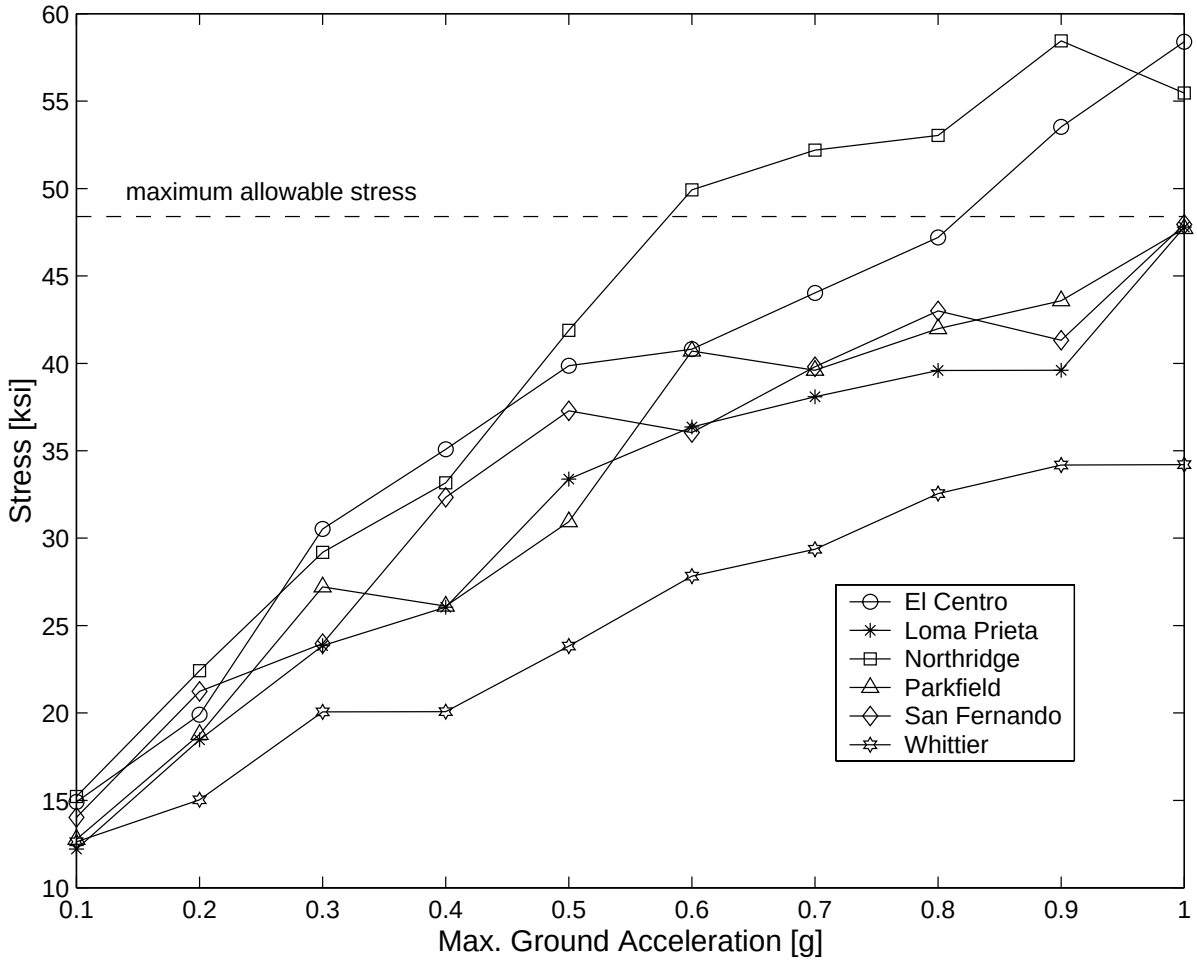

Figure 2.26 Maximum stress in the rail as a function of maximum ground acceleration for different earthquake inputs.

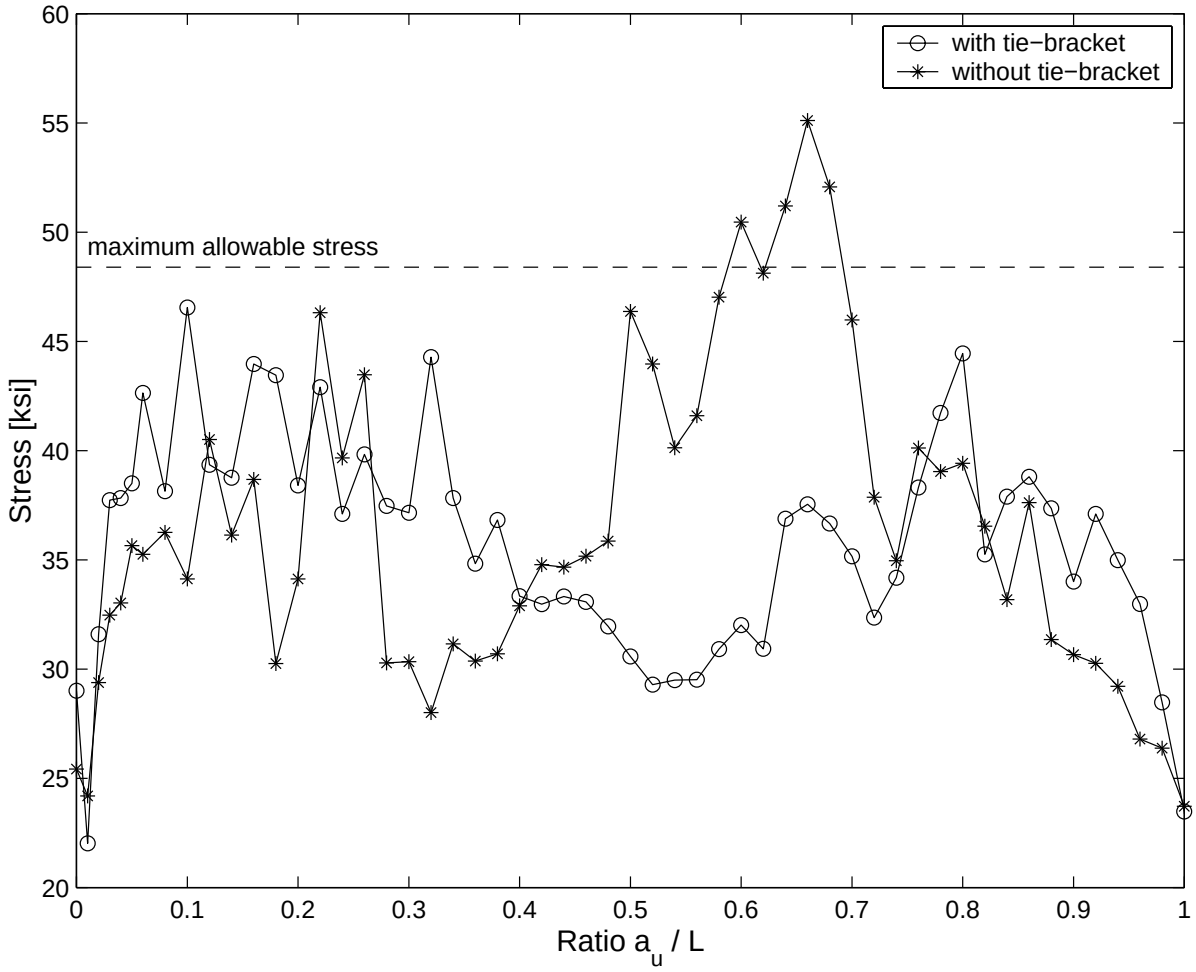

Figure 2.27 Maximum stress in the rail with and without intermediate tie-bracket for actual Northridge earthquake.

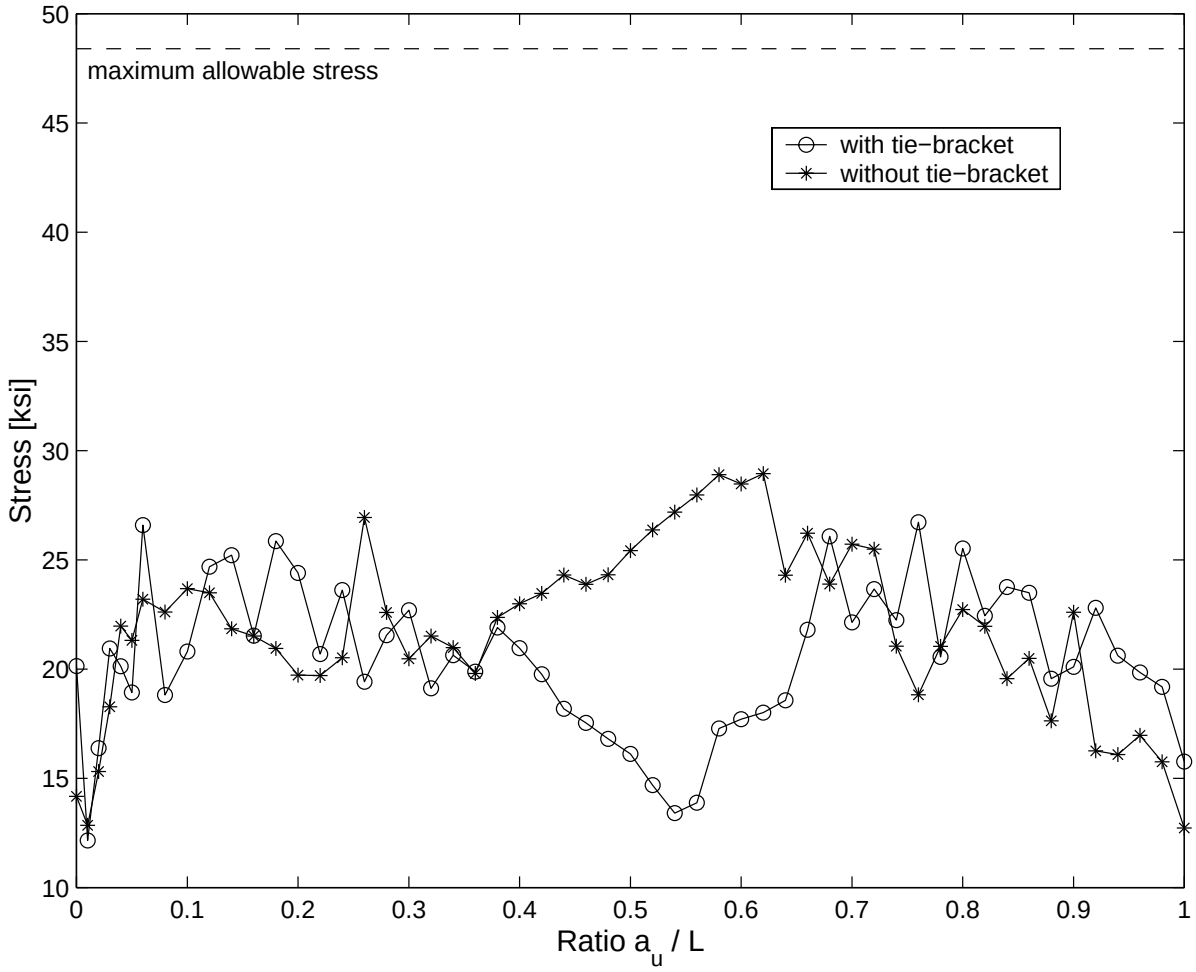

Figure 2.28 Maximum stress in the rail with and without intermediate tie-bracket for actual El Centro earthquake.

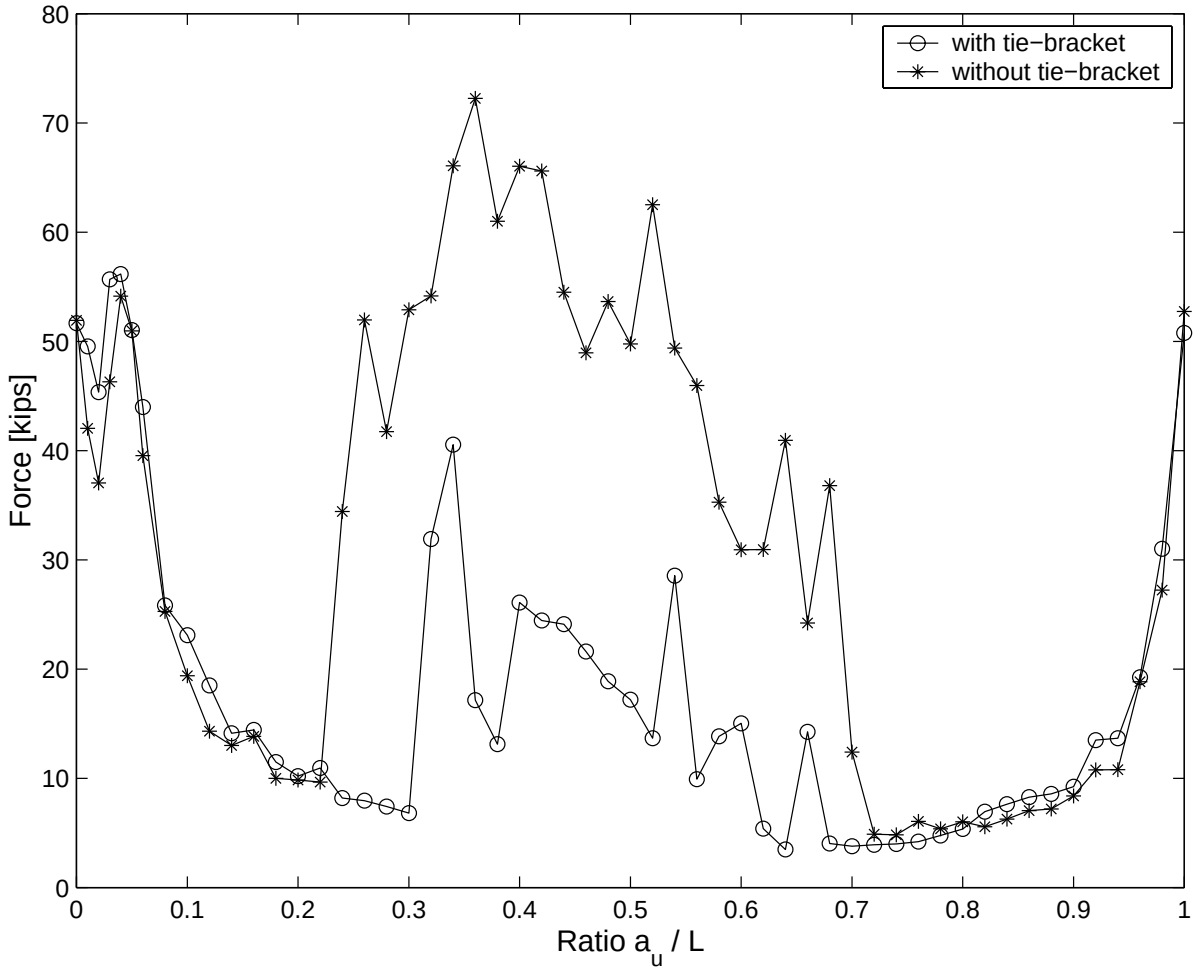

Figure 2.29 Maximum in-plane force in the bracket for the system with and without intermediate tie-bracket under actual Northridge earthquake.

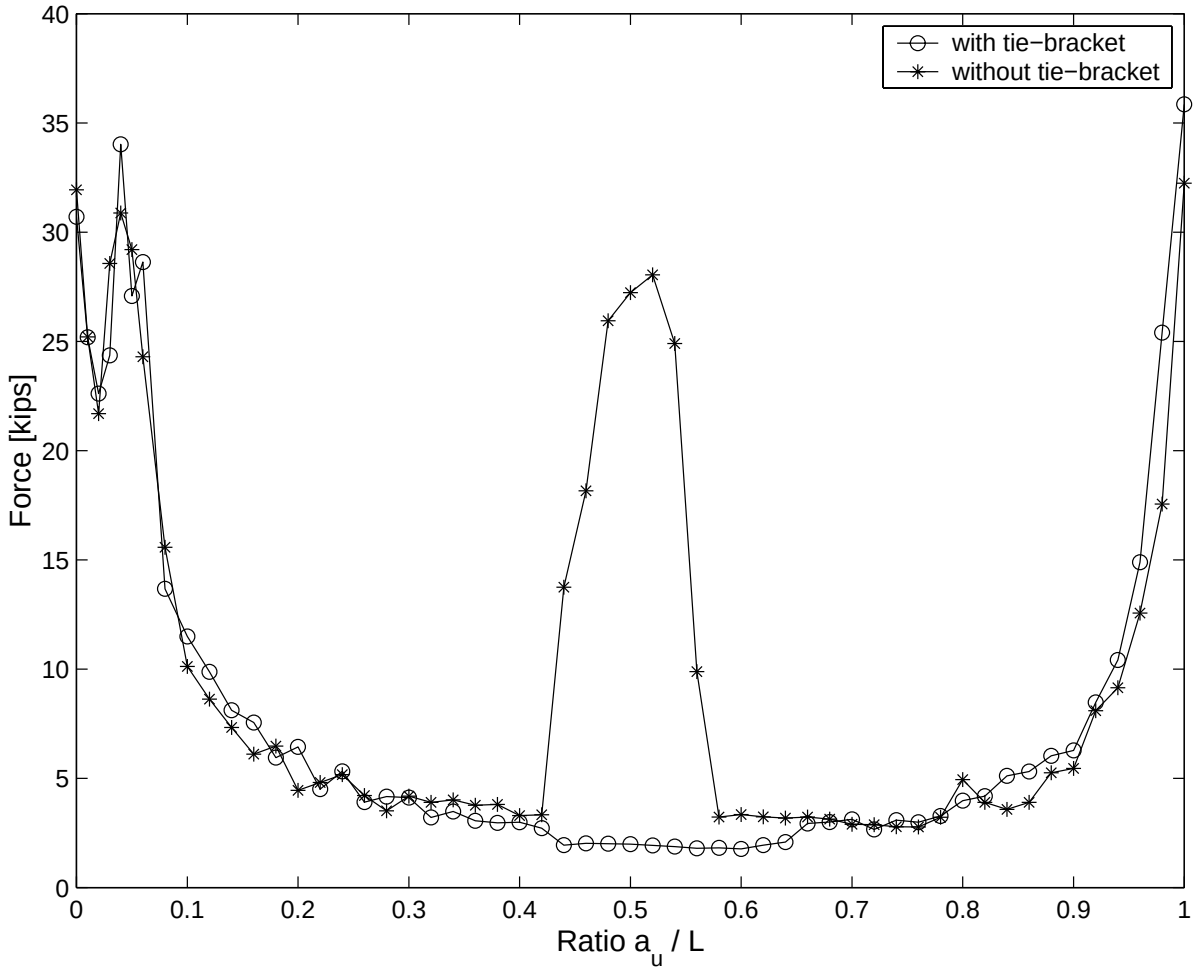

Figure 2.30 Maximum in-plane force in the bracket for the system with and without intermediate tie-bracket under actual El Centro earthquake.

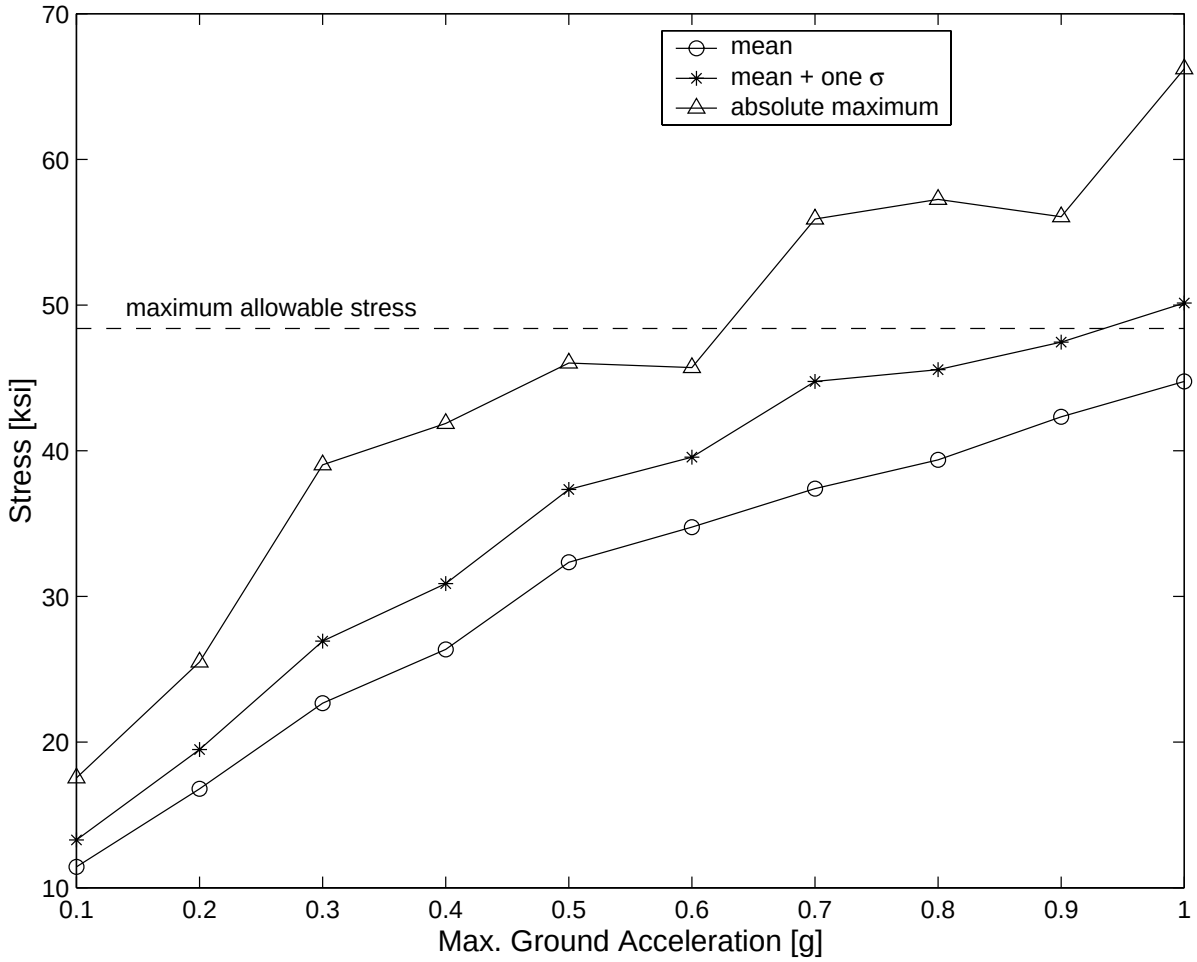

Figure 2.31 Statistics of peak stress in the rail under 50 synthetic ground motions.

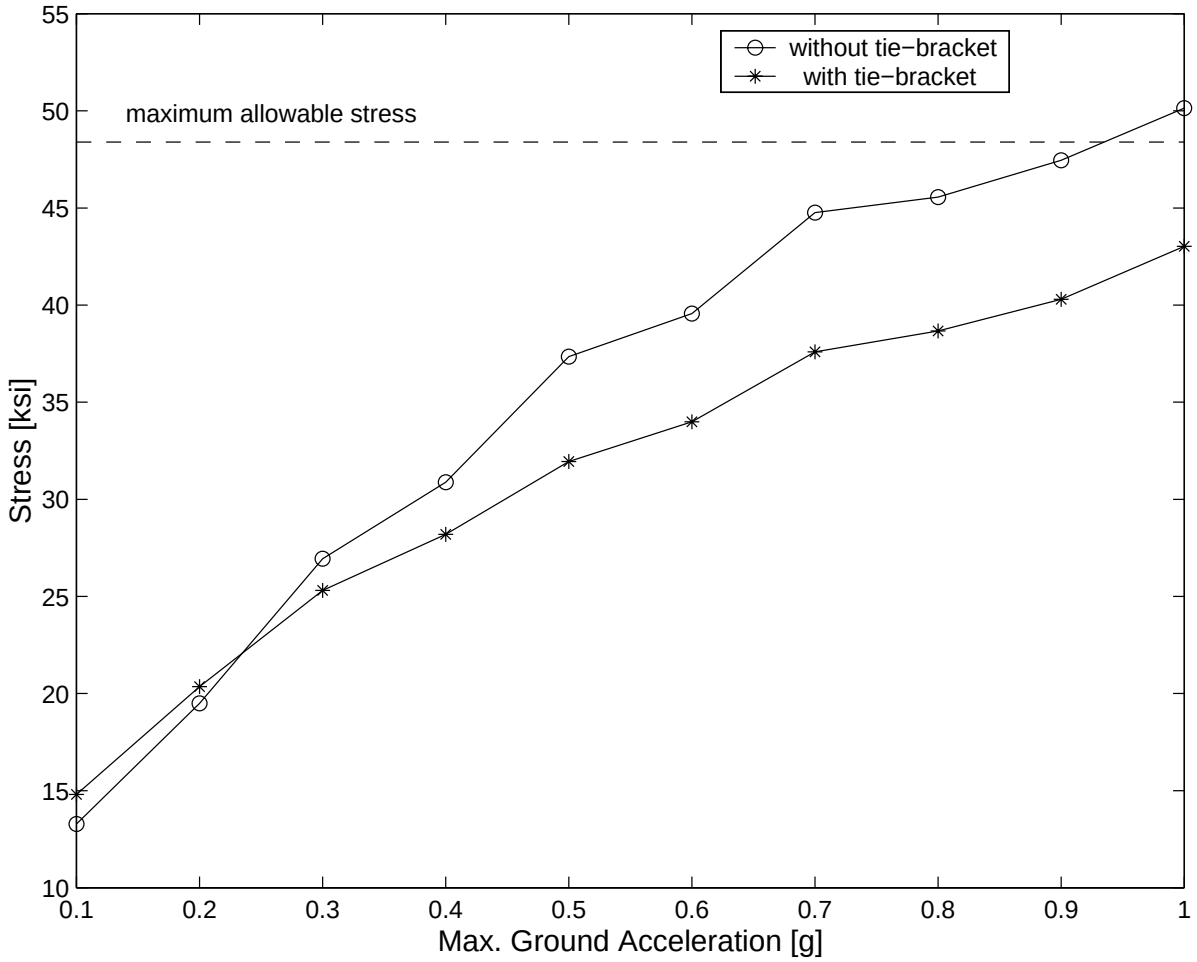

Figure 2.32 Mean plus one standard deviation of the peak stress in the rail for system with and without intermediate tie-bracket.

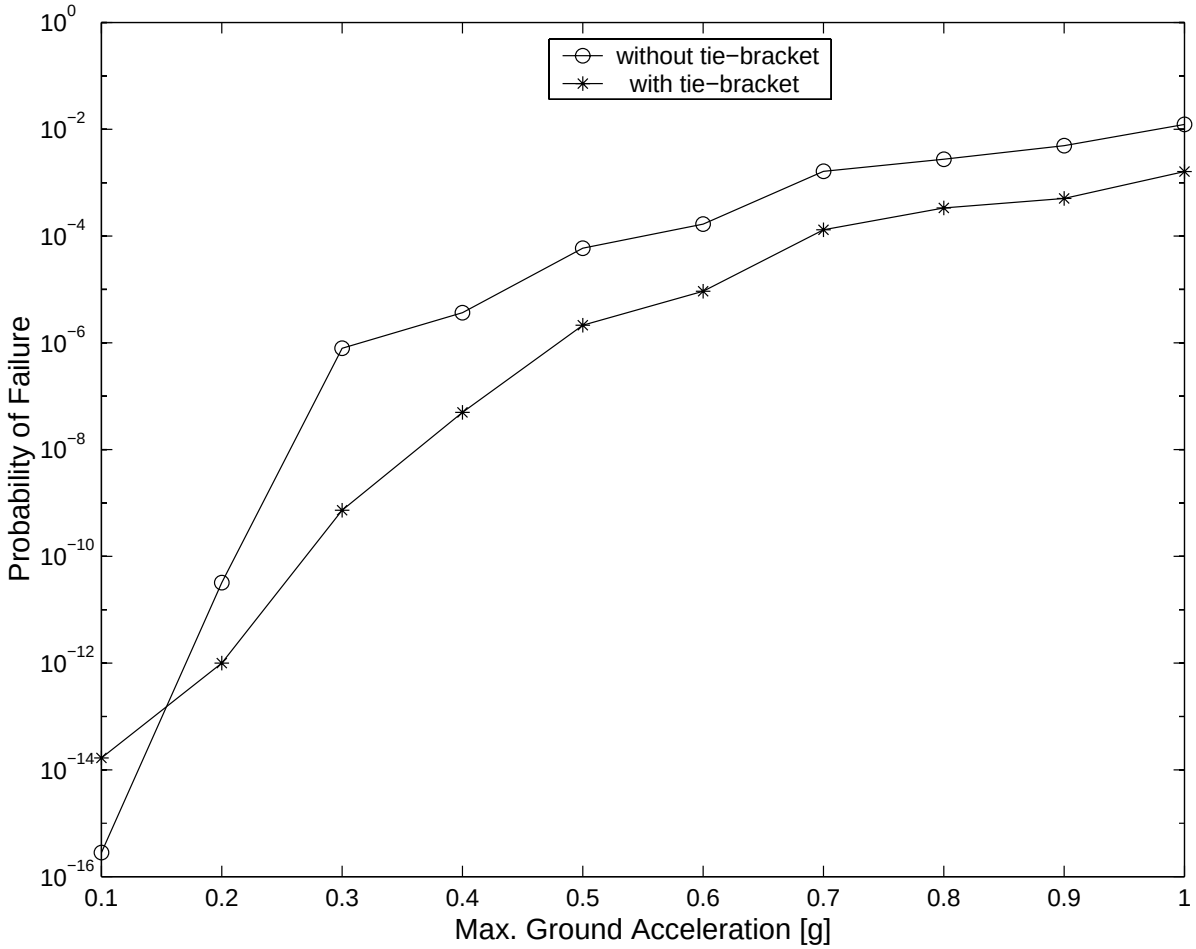

Figure 2.33 Fragility curves of system with and without intermediate tie-bracket.

Table 2.1 Properties of the 10-Story Torsional Building

Story	Mass	Inertia	Stiffness		Eccentricity	
	[10^3 lb.s^2/in]	[10^5 lb.in.s^2]	$k_x = k_y$ [10^6 lb/in]	k_t [10^{12} lb.in]	e_x [in]	e_y [in]
1	7.5260	1.4177	4.5855	2.3794	90	60.15
2	6.9145	1.3025	17.6904	9.7333	90	60.15
3	6.9145	1.3025	17.6904	9.7333	90	60.15
4	6.8163	1.2840	13.6469	6.8930	90	60.15
5	6.8163	1.2840	13.6469	6.8930	90	60.15
6	6.8163	1.2840	13.6469	6.8930	90	60.15
7	6.8163	1.2840	13.6469	6.8930	90	60.15
8	6.6634	1.2550	7.6896	3.7498	90	60.15
9	6.6634	1.2550	7.6896	3.7498	90	60.15
10	6.6634	1.2550	7.6896	3.7498	90	60.15

Table 2.2 Frequencies of the 10-Story Torsional Building

Mode	Frequency [rad/sec]	Period [sec]	Participation factor
1	5.70	1.1014	-139.0785
2	5.77	1.0892	208.1074
3	15.60	0.4027	-38.2893
4	15.78	0.3981	-57.2584
5	26.33	0.2386	-16.9277
6	26.63	0.2359	-25.3191
7	38.59	0.1628	-6.9129
8	39.04	0.1609	10.3518
9	47.78	0.1315	-4.7535
10	48.33	0.1300	7.1106
11	58.14	0.1081	2.9359
12	58.81	0.1068	-4.3990
13	63.23	0.0994	2.2669
14	63.96	0.0982	-3.3775
15	73.20	0.0858	-1.6666
16	74.04	0.0849	2.4912
17	83.40	0.0753	-0.7834
18	84.35	0.0745	1.1747
19	91.33	0.0688	0.9745
20	92.32	0.0681	-1.4548
21	967.84	0.0065	0.1229
22	2605.72	0.0024	0.0347
23	4400.36	0.0014	-0.0152
24	6454.48	0.00097	0.0059
25	8013.25	0.00078	-0.0042
26	9726.08	0.00065	-0.0024
27	10585.43	0.00059	0.0024
28	12336.80	0.00051	-0.0016
29	14035.72	0.00045	0.0006
30	15778.94	0.00040	0.0009

Table 2.3 Moment of inertia and distance from centroid to outermost point for standard T-sections for guide rail

Rail Size	**Moment of Inertia [in^4]**		**Distance c [in]**	
[lb/ft]	**I_{xx}**	**I_{yy}**	**c_x**	**c_y**
8	1.424	1.369	1.641	1.75
11	4.279	2.885	2.376	2.25
12	4.476	3.948	2.413	2.50
15	4.797	6.294	2.544	2.50
18.5	9.743	8.400	2.998	2.75
22.5	10.924	9.627	2.652	2.75
30	22.633	11.867	3.244	2.75

Table 2.4 Seismic inputs used in the study

Event	Date	Location	Max. Ground Acceleration [g]	
			x-direction	y-direction
El Centro	05/18/1940	Imperial Valley Irrigation District	0.348	0.214
Parkfield	06/27/1966	Cholame, Shandon, CA	0.434	0.355
San Fernando	02/09/1971	Pacoima Dam	1.170	1.075
Whittier	10/01/1987	Tarzana - Cedar Hill Nursery	0.537	0.405
Loma Prieta	10/17/1989	Corralitos - Eureka Canyon Rd.	0.630	0.478
Northridge	01/17/1994	Sylmar - County Hospital Parking Lot	0.843	0.604